Journal Pre-proofs

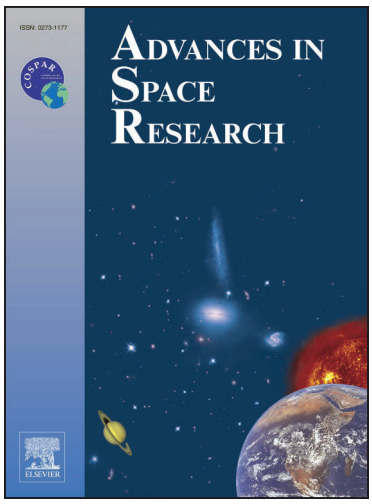

Probabilistic multi-dimensional debris cloud propagation subject to non-linear dynamics

Lorenzo Giudici, Mirko Trisolini, Camilla Colombo

PII: S0273-1177(23)00308-3
DOI: https://doi.org/10.1016/j.asr.2023.04.030
Reference: JASR 16675

To appear in: *Advances in Space Research*

Received Date: 27 October 2022
Accepted Date: 20 April 2023

Please cite this article as: Giudici, L., Trisolini, M., Colombo, C., Probabilistic multi-dimensional debris cloud propagation subject to non-linear dynamics, *Advances in Space Research* (2023), doi: https://doi.org/10.1016/j.asr.2023.04.030

Available online at www.sciencedirect.com

ScienceDirect

Advances in Space Research xx (2023) xxx-xxx

ADVANCES IN SPACE RESEARCH (a COSPAR publication)

www.elsevier.com/locate/asr

Probabilistic multi-dimensional debris cloud propagation subject to non-linear dynamics

Lorenzo Giudici[a,*], Mirko Trisolini[a], Camilla Colombo[a]

[a] *Politecnico di Milano, via La Masa 34, Milano 20156, Italy*

Abstract

The permanent power loss and the deviation of the trajectory of satellites impacted by centimetre and sub-centimetre sized debris have highlighted the need of taking into account such small fragments in the evolutionary models of the debris population and in the assessment of the in-orbit collision risk. When scaling down to the centimetre-millimetre range, deterministic models for propagating the fragments' orbit suffer from the massive computational cost required. The continuum approach for modelling the debris clouds is a well-established alternative to the piece-by-piece propagation. A density function is formulated to describe the distribution of fragments over a suitable phase space. Accurate and efficient continuum formulations have been developed to propagate clouds of fragments under atmospheric drag and J_2 perturbations, but a general model able to work under any dynamical regime has still to be found. This paper proposes a continuum approach that combines the method of characteristics with the discretisation of the domain in Keplerian elements and area-to-mass ratio into bins. The problem of using a binning approach with such a multi-dimensional phase space is addressed bounding and partitioning the domain, through probabilistic models on the way the fragments distribute over the phase space, as consequence of a fragmentation event. The proposed approach is applied to the modelling and propagation of a space debris cloud under the full set of orbital perturbations, and compared against a Monte Carlo simulation in terms of objects' number and distribution. The method proves to be accurate on the medium scale, in both space and time, and guarantees statistical validity with a reduced computational effort, leveraging its probabilistic nature.

Keywords: Space debris; Density distribution; Cloud propagation; Continuity equation

1. Introduction

The growing dependence of our daily lives on space services has caused a massive growth in space activities over the past decade. Since the early age of space exploration until 2016, the number of payloads launched in Low-Earth Orbit (LEO) remained below 200 per year; instead, over the last 5 years, this rate dramatically increased up to the almost 1800 payloads launched in 2021 (ESA Space Debris Office, 2021). According to the European Space Agency, approximately 30000 objects are regularly tracked by the Space Surveillance Network (ESA Space Debris Office, 2021). The trackability of objects in space is mainly affected by distance and size (McKnight & Di Pentino, 2013); in LEO, typically objects down to 5-10 cm can be monitored from ground, while in geostationary orbit only objects as big as 1 m are visible. As pointed out in Drolshagen (2008), millimetre sized particles can penetrate exposed tanks or seriously damage certain equipment, while even larger particles typically lead to the complete destruction of the impacted spacecraft part (Adushkin et al., 2020). Studies on the permanent partial power loss suffered by Sentinel-1A on 23/08/2016 seem to indicate that the satellite was impacted by a debris fragment with a mass comparable to an aluminum sphere with a diameter of 5 mm (Krag et al., 2017). The risk posed by small impacting debris was extensively analysed by Smirnov et al. (2015), who conducted experiments

*Corresponding author

Email addresses: lorenzo1.giudici@polimi.it (Lorenzo Giudici), mirko.trisolini@polimi.it (Mirko Trisolini), camilla.colombo@polimi.it (Camilla Colombo)

https://dx.doi.org/10.1016/j.jasr.xxxx.xx.xxx

to determine the crater depth as function of collision velocity and impactor size. In addition to the structural damage, every hyper-velocity impact creates plasma that might cause electromagnetic interference (Drolshagen, 2008). The possible hazard caused by such small fragments on operational satellites highlights the need of taking them into account in the evolutionary models of the space debris population and in the assessment of the risk on orbiting assets. Moreover, as motivated by Smirnov et al. (2020), the effect of mutual collisions between debris of various sizes might also be detrimental for the sustainability of the space environment. Deterministic approaches for the long-term propagation of space debris (Liou et al., 2004; Walker et al., 2001) are typically limited to fragments as large as 10 cm because of the massive computational time required. Including fragments down to the millimetre level demanded the introduction of simplifying assumptions on the fragments' dynamics and distribution, which allowed to address long-term propagation with a reasonable computational cost. The most viable approach demonstrated to be the characterisation of the debris fragments from a probabilistic perspective, which considers them no longer as single pieces but as a cloud. Chobotov (1990) modelled the early stage of the cloud volume evolution through the linearised equation for relative motion, for an efficient assessment of the collision risk posed by a fragmentation just after the breakup. The effect of the J_2 perturbation was also included for the short-term propagation of the cloud volume. Smirnov et al. (1993, 2001, 2002), and Nazarenko (1997), propagated the debris population in LEO by numerically solving the continuity equation, after having gathered the fragments into phases, depending on their physical properties and orbit type. In McInnes (1993, 1994), the first analytical model for propagating clouds of fragments under the effect of atmospheric drag was developed, applying the Method Of Charcteristics (MOC) to the continuity equation. The model considers the objects moving on quasi-circular orbits, which allows to describe the fragments' dynamics as function of orbital radius only. In Letizia et al. (2015a), the method was extended to a 2D model in semi-major axis a and eccentricity e. In order to keep the solution analytical, the effect of drag on fragments' eccentricity was neglected; nevertheless, the characterisation of the debris in the 2D phase space allowed to relax the constraint of circular orbit for the objects. Neglecting the effect of the Earth oblateness does not allow to describe the early stage of the cloud evolution (McKnight, 1990; Jehn, 1990), when the fragments form a band around the Earth under the effect of the J_2 perturbation. As a result, the cited analytical models numerically propagated the debris generated by a fragmentation event for a period of time after which the cloud can be assumed to be randomised in right ascension of the ascending node Ω and argument of periapsis ω, according to the Ashenberg approximation (Ashenberg, 1994). In Letizia et al. (2015c), the long-term effect of the Earth oblateness (Vallado & McClain, 2007) was included in the continuum formulation, describing the density of the orbiting objects in the 3D phase space (a, Ω, ω). As pointed out in Letizia et al. (2015c), neglecting other perturbations in the density-based modelling of space debris limits the applicability of the method to an altitude below 1000 km, above which Solar Radiation Pressure (SRP) and third-body (3B) perturbation become significant (Vallado & McClain, 2007). In Letizia (2018) it was possible to propagate clouds of fragments under the simultaneous effect of drag and SRP without eclipses, after band formation, by numerically solving the continuity equation through finite differences. In Frey et al. (2019), the Starling suite was proposed, a tool that potentially extends the continuum formulation to any dimensions and any non-linear dynamics. It numerically propagates the continuity equation along the characteristic lines, and retrieves the density distribution through a Gaussian Mixture Model (GMM), in the phase space of Keplerian elements and area-to-mass ratio. Hence, the applicability of the model is inherently linked to the possibility of describing the fragments' density as sum of Gaussian distributions. As motivated in Frey (2020), the method is not currently able to accommodate forces that lead to resonances on a small subset of the phase space, as it could be the case of 3B perturbation or SRP. Indeed, such resonances tend to generate bifurcations, which make it difficult to fit the distribution with a GMM.

This work aims at developing a method for the characterisation and propagation of fragments' clouds under any dynamical regime, through a continuum formulation. This objective is achieved combining the MOC with the discretisation of the phase space domain of Keplerian elements and area-to-mass ratio into bins, which is expected to be agnostic to the force model implemented. The main effort when dealing with a binning approach applied to such a multi-dimensional phase space is the computational cost. The problem is here addressed by estimating the way the fragments distribute over the phase space as consequence of a fragmentation event, by means of probabilistic models. This allows to bound the domain reachable by the ejected fragments, thus evaluating and propagating the debris' cloud only in the regions of the phase space, which are more likely to host the ejected fragments over time.

The paper is organised as follows:

- Section 2 proposes a novel approach to determine the phase space domain in the subset of independent Keplerian elements and area-to-mass ratio occupied by the fragments ejected by either an explosion or a collision in space. The accuracy of the mathematical model is tested on two fragmentation scenarios.

- Section 3 presents the method developed to estimate the fragments' distribution as consequence of a fragmentation event, through the partitioning of the computed phase space domain into bins. An innovative adaptive Monte Carlo integration method is implemented to address the problem of computational cost.

- Section 4 describes the dynamical model for the propagation of the fragments' density over time, through the application of the method of characteristics to the continuity equation. It also demonstrates how the unfolded distribution in the full set of Keplerian elements is obtained from the folded distribution in the subset of independent Keplerian elements, by imposing intersection between the frag-

ments' and parent orbit in the fragmentation point. Note that, in this work, the parent orbit refers to the osculating orbit of the fragmenting object (called parent object) at the epoch of the fragmentation.

- Section 5 details the approach to interpolate the propagated characteristics over the phase space of slow-varying Keplerian elements and area-to-mass ratio, through a binning approach. To improve the smoothness and continuity of the density distribution, an interpolation among neighbouring bins is also included.

- Section 6 is devoted to the application of the presented model to the modelling and propagation under the main orbital perturbations of a fragments' cloud, generated by a potential explosion of an Ariane 5 rocket body in a geostationary transfer orbit. The accuracy of the model is tested against a Monte Carlo simulation.

- Section 7 recaps the main results and achievements of the work.

2. Probabilistic domain of a breakup event

This section introduces an innovative method to bound the domain that the fragments ejected by either an in-orbit collision or explosion occupy. The proposed mathematical model takes as input a probabilistic breakup model and determines boundaries in area-to-mass ratio and ejection velocity, on the basis of the fraction of fragments that, on average, the model aids to characterise. The computed 2D domain is eventually mapped into a 4D domain in a subset of three independent Keplerian elements and area-to-mass ratio.

2.1. Breakup model

The NASA Standard Breakup Model (NASA SBM) (Johnson et al., 2001) is a semi-empirical model, which characterises the fragments generated by a collision or explosion in terms of characteristic length L, area-to-mass ratio A/M and ejection velocity Δv. In Frey & Colombo (2021), the model was reformulated in a probabilistic fashion, through the following Probability Density Functions (PDFs):

$$p_\lambda = \log(10)\,\beta \frac{10^{-\beta\lambda}}{10^{-\beta\lambda_0} - 10^{-\beta\lambda_1}} \tag{1a}$$

$$p_{\chi|\lambda} = \sum_i \alpha_i(\lambda)\,\mathcal{N}\left(\mu_\chi^{(i)}(\lambda), \sigma_\chi^{(i)}(\lambda)\right), \quad \sum_i \alpha_i(\lambda) = 1 \tag{1b}$$

$$p_{\nu|\chi} = \mathcal{N}\left(\mu_\nu(\chi), \sigma_\nu\right) \tag{1c}$$

where β is a unit-less parameter dependent on the type of fragmentation; λ, χ and ν are the logarithms to base 10 of the characteristic length L, area-to-mass ratio A/M and ejection velocity Δv, respectively; λ_0 and λ_1 are the logarithms to base 10 of lower L_0 and upper L_1 boundaries on the characteristic length; $\mu_\chi^{(i)}$, $\sigma_\chi^{(i)}$, μ_ν and σ_ν are mean and standard deviation of normal distributions $\mathcal{N}$ in χ and ν, which depend on the type of fragmentation; α_i are factors to weight the relative importance of the normal distributions in the conditional probability in χ dependent on λ. The conditional PDFs of Eqs. (1) are used to bound the domain that is probabilistically reachable by the ejected fragments.

2.2. Limit values in ejection velocity and area-to-mass ratio

The desired phase space domain is defined in Keplerian elements and area-to-mass ratio, which, according to the dynamical model adopted in this work (Section 4), represent the set of variables needed for propagating the cloud of fragments. Hence, the information on the distribution of the fragments in characteristic length is filtered out through marginalisation. On the other hand, the knowledge on how the fragments are distributed in area-to-mass ratio is crucial from a cloud dynamics point of view; indeed, atmospheric drag and solar radiation pressure perturbations are strongly affected by this parameter. In this section, boundaries in ejection velocity and area-to-mass ratio are identified by considering the Cumulative Density Functions (CDFs) in logarithm to base 10 of area-to-mass ratio χ, and ejection velocity ν.

The CDF in χ, $F_\chi(\chi)$, can be computed from the joint probability $p_{\chi,\lambda}$, as follows.

$$F_\chi(\chi) = \int_{-\infty}^{\chi}\int_{\lambda_0}^{\lambda_1} p_{\chi|\lambda} p_\lambda \,\mathrm{d}\lambda\,\mathrm{d}\chi \tag{2}$$

If χ_0 and χ_{N_χ} are the boundaries of the domain in χ, $\mathcal{D}_\chi$, the probability P_χ for a fragment to be in the semi-closed interval $\left(\chi_0, \chi_{N_\chi}\right]$ is:

$$P_\chi\left(\chi_0 < \chi \leq \chi_{N_\chi}\right) = F_\chi\left(\chi_{N_\chi}\right) - F_\chi(\chi_0) \tag{3}$$

Imposing a limit $\xi \in [0, 1)$ to the fraction of fragments probabilistically included in the domain $\mathcal{D}_\chi$, the two limit values χ_0 and χ_{N_χ} can be found solving the following system:

$$\begin{cases} P_\chi\left(\chi_0 < \chi \leq \chi_{N_\chi}\right) = \xi \\ p_\chi(\chi_0) = p_\chi\left(\chi_{N_\chi}\right) \end{cases}, \quad p_\chi = \int_{\lambda_0}^{\lambda_1} p_{\chi|\lambda} p_\lambda \,\mathrm{d}\lambda \tag{4}$$

where the second equation of the system imposes the same density value at the boundary of the domain, which allows to frame the range in χ with the highest probability of collecting debris fragments. Indeed, note that the constraint of the first equality of Eq. (4) may be fulfilled by an infinite couple of limit values, χ_0 and χ_{N_χ}, satisfying:

$$\begin{cases} F_\chi(\chi_0) < 1 - \xi \\ F_\chi\left(\chi_{N_\chi}\right) > \xi \end{cases} \tag{5}$$

Nevertheless, the solution of Eq. (4) is the only one providing a balanced distribution, that gives the same relevance to low and high area-to-mass ratio fragments. In other words, if the PDF p_χ were a normal distribution, the second equation would impose that χ_0 and χ_{N_χ} were at the same distance with respect to the mean value, allowing the identification of the domain with the highest probability of hosting an ejected fragment.

The CDF in logarithm to base 10 of ejection velocity v, $F_v(v)$, can be computed as:

$$F_v(v) = \int_{-\infty}^{v} \int_{-\infty}^{\infty} p_{v|\chi} p_\chi \, \mathrm{d}\chi \, \mathrm{d}v \tag{6}$$

By imposing that $\chi \in \mathcal{D}_\chi$, the probability P_v for a fragment to be ejected with an ejection velocity $\overline{\Delta v} \leq 10^{\overline{v}}$, can be obtained as:

$$P_v(v \leq \overline{v}) = \int_{-\infty}^{\overline{v}} \int_{\chi_0}^{\chi_{N_\chi}} p_{v|\chi} p_\chi \, \mathrm{d}\chi \, \mathrm{d}v, \quad P(v \leq \overline{v}) \in [0, \xi) \tag{7}$$

Note that, with respect to the approach followed for setting the limits in χ, for the ejection velocity only the upper limit is constrained. This is because when including the direction of the impulse and transforming the limits in ejection velocity into boundaries in Keplerian elements, the left bound would be anyway lost. Indeed, consider that, even with a high ejection velocity, one may get a zero variation of inclination if the ejection velocity vector lies on the orbital plane. Therefore, the distribution in v is here only right bounded.

If the domain in logarithm to base 10 of area-to-mass ratio χ, $\mathcal{D}_\chi$, is discretised into N_χ bins, the inner integral of Eq. (7) can be written as a summation of integrals over the bins in χ, as follows.

$$P_v(v \leq \overline{v}) = \int_{-\infty}^{\overline{v}} \sum_{j=1}^{N_\chi} \int_{\chi_{j-1}}^{\chi_j} p_{v|\chi} p_\chi \, \mathrm{d}\chi \, \mathrm{d}v \tag{8}$$

with:

$$\chi_n = \chi_0 + \sum_{j=1}^{n} \delta\chi_j \tag{9}$$

Assuming the conditional probability density function $p_{v|\chi}$ to be independent of χ over a step $\delta\chi_j$ in χ, allows to take it out of the first integral. It is assumed that:

$$p_{v|\chi}(v, \chi) \approx p_{v|\chi}\left(v, \overline{\chi}_j\right) \quad \forall \chi \in \left[\chi_{j-1}, \chi_j\right) \tag{10}$$

with:

$$\overline{\chi}_j = \frac{\chi_{j-1} + \chi_j}{2} \tag{11}$$

Plugging Eqs. (1c) and (10) into Eq. (8), it transforms as follows.

$$P_v(v \leq \overline{v}) = \sum_{j=1}^{N_\chi} \Phi^{(j)}(\overline{v}) \, P_\chi\left(\chi_{j-1} < \chi \leq \chi_j\right) \tag{12}$$

where Φ indicates the CDF of a normal distribution and $\Phi^{(j)}(\overline{v})$ is defined as:

$$\Phi^{(j)}(\overline{v}) = \int_{-\infty}^{\overline{v}} p_{v|\chi}\left(v, \overline{\chi}_j\right) \, \mathrm{d}v \tag{13}$$

With an abuse of notation, considering different limits in logarithm to base 10 of ejection velocity v for each bin in χ, Eq. (12) modifies as follows.

$$P_v(\boldsymbol{v} \leq \overline{\boldsymbol{v}}) = \sum_{j=1}^{N_\chi} \Phi^{(j)}\left(v_j\right) P_\chi\left(\chi_{j-1} < \chi \leq \chi_j\right) \tag{14}$$

which allows the domain to be bounded in ejection velocity independently for each area-to-mass ratio bin, leading to N_χ domains $\mathcal{D}_v^{(j)}$ in v. Calling ζ the fraction of fragments which the model probabilistically aims to characterise, the N_χ boundary values in v, $\overline{v}_j$, and 2 boundary values in χ, χ_0 and χ_{N_χ}, must satisfy the relation:

$$\begin{cases} \sum_{j=1}^{N_\chi} \Phi^{(j)}\left(v_j\right) P_\chi\left(\chi_{j-1} < \chi \leq \chi_j\right) = \zeta, \quad \zeta \in [0, \xi) \\ P_\chi\left(\chi_0 < \chi \leq \chi_{N_\chi}\right) = \xi, \quad \xi \in [0, 1) \\ p_\chi\left(\chi_0\right) = p_\chi\left(\chi_{N_\chi}\right) \end{cases} \tag{15}$$

Eq. (15) is a system of 3 scalar equations in $N_\chi + 2$ unknowns. It is reasonable to ask for the same density level at the edges of the 2D domain $\mathcal{D}_{\chi,v}$ in (χ, v); indeed, so far, Eq. (15) is only constraining the overall targeted accuracy level, which one may obtain tuning differently the boundary values χ_0, χ_{N_χ} and v_j. This further consideration allows retrieving the missing $N_\chi - 1$ equations, imposing the following constraint:

$$p_{v,\chi}(v, \chi) \geq \overline{p}_{v,\chi}(\zeta), \quad \forall (\chi, v) \in \mathcal{D}_{\chi,v} \tag{16}$$

Eq. (16) constrains the PDF $p_{v,\chi}$ in any point $(v, \chi) \in \mathcal{D}_{\chi,v}$ to be higher than a limit value $\overline{p}_{v,\chi}$, which depends on the fraction of fragments ζ.

Pursuing the same approach described previously, the bins in χ are considered separately and the conditional distribution $p_{v,\chi}$ is approximated according to Eq. (10). Under these assumptions, Eq. (16) modifies, as follows.

$$p_{v|\chi}\left(v, \overline{\chi}_j\right) p_\chi(\chi) \geq \overline{p}_{v,\chi}(\zeta), \quad j = 1, \ldots, N_\chi \tag{17}$$

An additional assumption is held to let Eq. (17) be function of v only; the density value p_χ is considered constant and equal to the mean value $\overline{p}_\chi^{(j)}$ over each bin in χ, which allows modifying Eq. (17) as:

$$p_{v|\chi}\left(v, \overline{\chi}_j\right) \frac{P_\chi\left(\chi_{j-1} < \chi \leq \chi_j\right)}{\delta\chi_j} \geq \overline{p}_{v,\chi}(\zeta), \quad j = 1, \ldots, N_\chi \tag{18}$$

where the integral mean rule has been applied. Finally, it is imposed that, for each area-to-mass ratio bin, the density value at the edges of the domain must coincide, i.e.:

$$p_{v|\chi}\left(v_j, \overline{\chi}_j\right) \frac{P_\chi\left(\chi_{j-1} < \chi \leq \chi_j\right)}{\delta\chi_j} = \overline{p}_{v,\chi}(\zeta), \quad j = 1, \ldots, N_\chi \tag{19}$$

where, with respect to Eq. (18), the conditional distribution $p_{v|\chi}$ is evaluated at the limit value of ejection velocity v_j. The constraint of Eq. (19) allows retrieving $N_\chi - 1$ equations of the kind:

$$p_{v|\chi}\left(v_j, \overline{\chi}_j\right) \overline{p}_\chi^{(j)} = p_{v|\chi}\left(v_{j+1}, \overline{\chi}_{j+1}\right) \overline{p}_\chi^{(j+1)} \tag{20}$$

with:

$$\overline{p}_\chi^{(j)} = \frac{P_\chi\left(\chi_{j-1} < \chi \leq \chi_j\right)}{\delta\chi_j} \tag{21a}$$

$$\overline{p}_\chi^{(j+1)} = \frac{P_\chi\left(\chi_j < \chi \leq \chi_{j+1}\right)}{\delta\chi_{j+1}} \tag{21b}$$

The parameters ξ and ζ are set to give the same weight to the distributions in logarithm to base 10 of area-to-mass ratio χ and ejection velocity ν, or, equivalently, to get the same integral of the marginalised distributions in χ and ν, between the computed limits. If the PDF in ν were a normal distribution independent of χ, p^*_ν, the parameter ζ could have been explicitly written as:

$$\zeta = \xi \cdot \eta \tag{22}$$

where η is the hypothetical cumulative density function in ejection velocity ν, F^*_ν, evaluated at the limit value $\overline{\nu}$. Remembering that the distributions in ν are only right-bounded, to equally weight the two PDFs in χ and ν, η must be set as:

$$\eta = F_\chi\left(\chi_{N_\chi}\right) = F^*_\nu\left(\overline{\nu}\right) = \frac{1+\xi}{2} \tag{23}$$

Hence, according to this analogy, the parameter ζ is constrained to be:

$$\zeta = \frac{1}{2}\xi\left(\xi+1\right) \tag{24}$$

or, inversely:

$$\xi = \frac{\sqrt{1+8\zeta}}{2} - \frac{1}{2} \tag{25}$$

Combining Eqs. (15), (20 and (25) the final system of $N_\chi + 2$ equations in $N_\chi + 2$ unknowns is found to be:

$$\begin{cases} \sum_{j=1}^{N_\chi} \Phi^{(j)}\left(\nu_j\right) P_\chi\left(\chi_{j-1} < \chi \leq \chi_j\right) = \zeta \\ p_{\nu|\chi}\left(\nu_1, \overline{\chi}_1\right) \overline{p}^{(1)}_\chi = p_{\nu|\chi}\left(\nu_2, \overline{\chi}_2\right) \overline{p}^{(2)}_\chi \\ \qquad \vdots \\ p_{\nu|\chi}\left(\nu_{N_\chi-1}, \overline{\chi}_{N_\chi-1}\right) \overline{p}^{(N_\chi-1)}_\chi = p_{\nu|\chi}\left(\nu_{N_\chi}, \overline{\chi}_{N_\chi}\right) \overline{p}^{(N_\chi)}_\chi \\ P_\chi\left(\chi_0 < \chi \leq \chi_{N_\chi}\right) = \frac{\sqrt{1+8\zeta}}{2} - \frac{1}{2} \\ p_\chi\left(\chi_0\right) = p_\chi\left(\chi_{N_\chi}\right) \end{cases} \tag{26}$$

Note that the 2 equations (Eqs. (4)) to find the 2 limits on χ, χ_0 and χ_{N_χ}, do not consider any simplifying assumption. On the other hand, the other N_χ equations approximate the conditional distribution $p_{\nu|\chi}$ in each bin in χ according to Eq. (10). Therefore, it was found to be more efficient to solve the two subset of equations with two different approaches. The solutions of Eqs. (4), which are independent of the remaining equations, are obtained through a root finding routine. Instead, the N_χ limits for the ejection velocity ν_j are computed by means of a non-linear programming algorithm, which aims to minimise the cost function J, corresponding to the first equation in Eq. (26):

$$J = \left| \sum_{j=1}^{N_\chi} \Phi^{(j)}\left(\nu_j\right) P_\chi\left(\chi_{j-1} < \chi \leq \chi_j\right) - \zeta \right| \tag{27}$$

under $N_\chi - 1$ equality constraints provided by the $N_\chi - 1$ equations of the form of Eq. (20). It is worth highlighting that the convergence of the minimisation process is affected by the step-size adopted for the bins in χ. Indeed, the larger the step-size is, the coarser the approximation of Eq. (10) becomes.

In the following, Eq. (26) is validated in two different scenarios: the explosion of a rocket body and a catastrophic collisions. For both the cases, the lower L_0 and upper L_1 boundaries on the characteristic length are set to 1 cm and 1 m, respectively. In the explosion case, the parameter S (Johnson et al., 2001) is set to 1, while an equivalent mass M_e of 1000 kg is assumed for the collision scenario.

2.2.1. Rocket body explosion

Figure 1 shows the 2D distribution in (χ, ν) at breakup. Note that the probability density function $p_{\nu,\chi}$ is here multiplied by the total number of generated fragments N, which, according to the NASA SBM, is 9503.

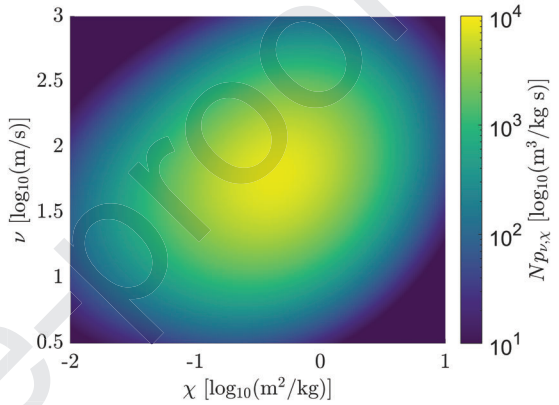

Fig. 1: Density distribution in (χ, ν) for a rocket body explosion.

Eq. (26) is solved with 20 bins in χ and setting the parameter ζ to 0.95, which means that the model is expected to characterise 95% of the generated fragments. In order to validate the approach proposed in Section 2.2, the limit value $\overline{p}_{\nu,\chi}(\zeta)$ of Eq. (19) is found numerically solving:

$$\overline{p}_{\nu,\chi}(\zeta) : \int_{\overline{p}_{\nu,\chi}(\zeta)}^{\infty} \mathrm{d}p_{\nu,\chi} = \zeta \tag{28}$$

Wherever the density value is lower than the value of Eq. (28), it is set equal to zero. The modified heatmap is depicted in Figure 2, together with the 2 boundary values in χ, χ_0 and χ_{N_χ}, and 20 limits in ν, ν_j. In Table 1 the convergence results of the root finding and minimisation processes are reported.

As it can be observed, the boundaries in χ capture almost all the remaining distribution, expect for two small circular segments, where, however, the range in ejection velocity is collapsing toward one point. The limit values in ν, instead, accurately follow the upper edge of the distribution.

2.2.2. Catastrophic collision

Figure 3 presents the density distribution in (χ, ν) for the catastrophic collision, from which 46755 fragments are generated. As it can be noticed, it remarkably differs from the one shown in Figure 1, both in shape and magnitude. Collisions normally generate a vast population of very small fragments with high relative velocities (Barrows et al., 1996). In particular, the edges of the distribution reach considerable ejection velocity values, which would inject a vast part of the cloud into

Table 1: Convergence results of the root finding and minimisation processes for a rocket body explosion.

Function	Value
$P_\chi\left(\chi_0 < \chi \leq \chi_{N_\chi}\right) - \xi$	$1.33 \cdot 10^{-15}$
$p_\chi\left(\chi_0\right) - p_\chi\left(\chi_{N_\chi}\right)$	$5.93 \cdot 10^{-14}$
J_{opt}	$4.65 \cdot 10^{-11}$
$\max_{j=1,\dots,N_\chi} \left\lvert p_{\nu\vert\chi}\left(\nu_j, \overline{\chi}_j\right)\overline{p}_\chi^{(j)} - p_{\nu\vert\chi}\left(\nu_{j+1}, \overline{\chi}_{j+1}\right)\overline{p}_\chi^{(j+1)}\right\rvert$	$4.77 \cdot 10^{-8}$

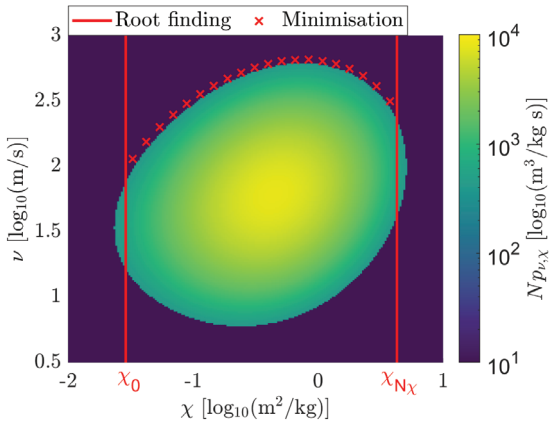

Fig. 2: Density distribution in (χ, ν) for a rocket body explosion - Density values greater than $\overline{p}_{\nu,\chi}(\zeta = 0.95)$.

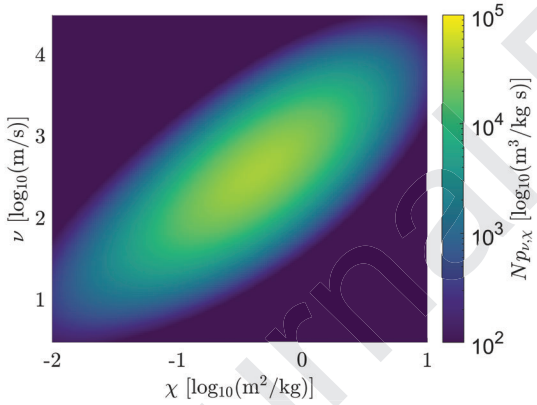

Fig. 3: Density distribution in (χ, ν) for a catastrophic collision.

hyperbolic trajectories. For this reason, the parameter ζ is here preferably set to 0.85, thus loosing 15% of the cloud.

Following the same approach proposed in Section 2.2.1, in Figure 4 is depicted the modified heatmap with the density values $p_{\nu,\chi} > \overline{p}_{\nu,\chi}(\zeta = 0.85)$, together with the limits in χ and ν, while in Table 2 are reported the convergence results.

As it can be inferred, also in this second scenario the validity of the model is guaranteed.

2.3. Domain in Keplerian elements and area-to-mass ratio

The objective of this section is to define domains in Keplerian elements associated to each area-to-mass ratio bin, through a one-to-one correspondence that maps each ejection velocity limit $\Delta v_j = 10^{\nu_j}$ into boundaries in Keplerian elements. The

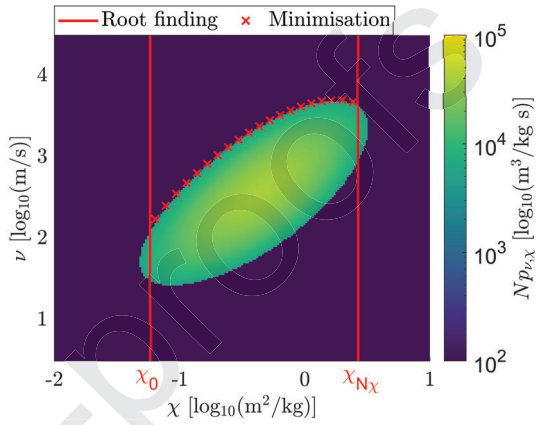

Fig. 4: Density distribution in (χ, ν) for a catastrophic collision - Density values greater than $\overline{p}_{\nu,\chi}(\zeta = 0.85)$.

NASA SBM does not provide any information on the distribution of the ejection velocity direction; therefore, as commonly done in the literature (Letizia et al., 2015b), the ejection velocity is here assumed to be isotropically distributed in direction. The ejection velocity vector $\boldsymbol{\Delta v}$ can be written as function of the magnitude Δv, in-plane γ and out-of-plane φ angles, which in this paper are defined with respect to the radial–transversal–out-of-plane (RSW) reference frame, as follows.

$$\boldsymbol{\Delta v} = \begin{Bmatrix} \Delta v \cos\gamma \cos\varphi \\ \Delta v \sin\gamma \cos\varphi \\ \Delta v \sin\varphi \end{Bmatrix} \tag{29}$$

As demonstrated in Frey & Colombo (2021), the PDFs in γ, p_γ, and φ, p_φ, are defined as:

$$p_\gamma = \frac{1}{2\pi} \tag{30a}$$

$$p_\varphi = \frac{\cos\varphi}{2} \tag{30b}$$

As it can be inferred, the in-plane angle γ is uniformly distributed over $[0, 2\pi)$, while the out-of-plane angle φ is not uniformly distributed. Hence, the directional velocity distribution $p_{\nu,\gamma,\varphi}$ can be computed as:

$$p_{\nu,\gamma,\varphi} = p_\nu \frac{\cos\varphi}{4\pi} \tag{31}$$

In Figure 5, the directional velocity distribution for a rocket body explosion is shown. Note that the density values correspond to a fixed value of χ.

As it can be noticed, the density value $p_{\nu,\chi,\gamma,\varphi}$ varies only as function of the ejection velocity magnitude Δv and out-of-plane angle φ, while it is constant over the in-plane angle γ.

Table 2: Convergence results of the root finding and minimisation processes for a catastrophic collision.

Function	**Value**
$P_\chi\left(\chi_0 < \chi \leq \chi_{N_\chi}\right) - \xi$	$-1.08 \cdot 10^{-14}$
$p_\chi\left(\chi_0\right) - p_\chi\left(\chi_{N_\chi}\right)$	$4.31 \cdot 10^{-13}$
J_{opt}	$2.47 \cdot 10^{-7}$
$\max_{j=1,\dots,N_\chi} \left\lvert p_{\nu\lvert\chi}\left(\nu_j, \overline{\chi}_j\right) \overline{p}_\chi^{(j)} - p_{\nu\lvert\chi}\left(\nu_{j+1}, \overline{\chi}_{j+1}\right) \overline{p}_\chi^{(j+1)} \right\rvert$	$1.84 \cdot 10^{-9}$

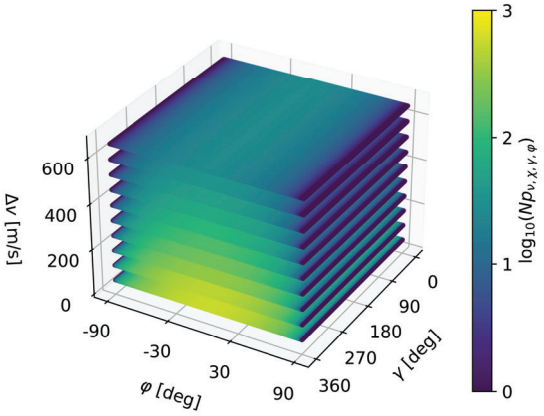

Fig. 5: Density distribution $p_{v,\chi,\gamma,\varphi}$ as function of ejection velocity magnitude Δv and angles γ, φ.

2.3.1. *Dimensionality-preserving Cartesian to Keplerian density transformation*

When the fragmentation occurs, the generated fragments are assumed to share the same initial position, but to have a velocity that depends on the impulse they receive. Therefore, the fragments are distributed according to a 4D density function in relative velocity and area-to-mass ratio only. When moving to a distribution in Keplerian elements, the same dimensionality is preserved; hence, the transformed distribution will be in a subset of three Keplerian elements and area-to-mass ratio (Frey & Colombo, 2021). The remaining dependent Keplerian elements are function of the independent ones and of the fragmentation point location. The same concept can be analysed from another perspective: since no uncertainty on the initial position is considered, the orbits of the generated fragments must intersect the orbit of the parent object in the fragmentation point. This means that the new orbits have only three degrees of freedom, that can freely vary in the domain that satisfies the constraint on velocity:

$$\Delta v\left(\chi\right) \leq 10^{\nu_j}, \quad \chi \in \left[\chi_{j-1}, \chi_j\right) \tag{32}$$

Let us consider the 3D distribution in ejection velocity depicted in Figure 5. Equally-spaced samples are extracted from the distribution and each ejection velocity vector is summed to the fragmentation Cartesian coordinates, keeping fixed the position vector. For each sample, the density value is retrieved according to Eq. (1). The set of Cartesian states is eventually converted into Keplerian elements (Vallado & McClain, 2007). The transformed samples' coordinates are plotted in Figure 6, separating the states in the two subsets (a, e, f) and $(i, \Omega, u = \omega + f)$, where a is semi-major axis, e eccentricity, i inclination, Ω right ascension of the ascending node, ω argument of periapsis, f true anomaly, and u argument of latitude. The following parent orbit Keplerian elements are considered, which correspond to the elements of the satellite Cosmos-2292: $a_P = 7554.5$ km, $e_P = 0.1025$, $i_P = 82.99$ deg, $\Omega_P = 154.77$ deg, $\omega_P = 264.28$ deg, and $f_P = 120$ deg, which is arbitrarily set. Note that, the area-to-mass ratio is considered fixed; indeed, the objective here is to demonstrate that, even though the transformation moves from the 3D space of ejection velocity to the 6D space of Keplerian elements, the transformation of the density distribution is dimension-preserving.

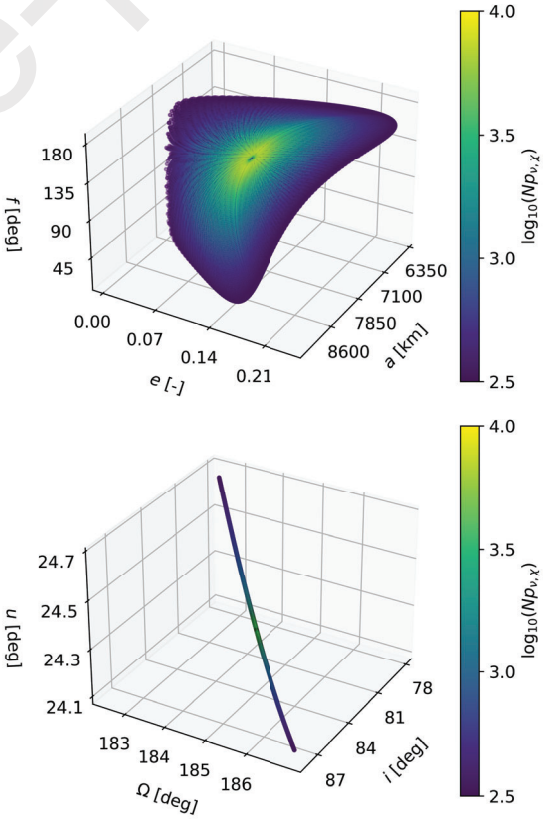

Fig. 6: Density distribution $p_{v,\chi}$ as function of the Keplerian elements.

As it can be noticed, even though the transformed distribution is function of the six Keplerian elements, it still remains a 3D distribution, composed by a line- and a surface-like distributions. The choice of the two subsets of orbital elements, which allows to graphically prove that the transformation preserves the dimensionality of the density distribution, was driven by the

constraints that the Keplerian elements must satisfy. The orbital radius equation (Vallado & McClain, 2007) provides a relation between semi-major axis a, eccentricity e and true anomaly f:

$$r = \frac{a\left(1-e^2\right)}{1+e\cos f} \tag{33}$$

where $r = r_P$ is the parent object's orbital radius at the epoch of the fragmentation. On the other hand, the sine and cotangent rules applied to the spherical triangle of Figure 7, link inclination, i, right ascension of the ascending node, Ω, and argument of latitude, u, as follows.

$$\frac{\sin u_P}{\sin i} = \frac{\sin u}{\sin i_P} \tag{34a}$$

$$\cos\Delta\Omega\cos i_P = \cot u_P \sin\Delta\Omega - \cot i \sin i_P \tag{34b}$$

where $\Delta\Omega = \Omega - \Omega_P$, and i_P, Ω_P, and u_P are the parent orbit inclination, right ascension of the ascending node, and argument of latitude, respectively.

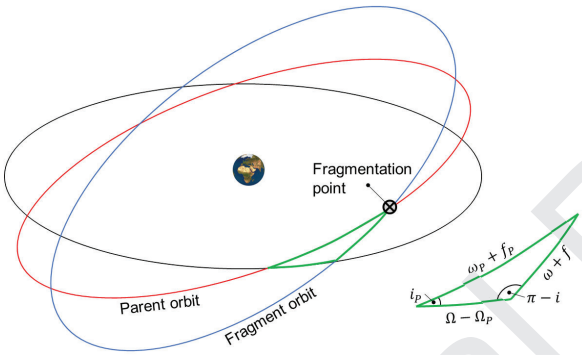

Fig. 7: Intersection between parent and fragments orbit.

The choice of the set of three independent Keplerian elements $\boldsymbol{\alpha}_i$ is arbitrary, but not all the combinations are possible. Indeed, $\boldsymbol{\alpha}_i$ must contain one element specifying the orientation of the orbital plane (i.e., either i or Ω) and ω and f cannot be taken together (Frey & Colombo, 2021). Here the subset (a, e, i) is chosen. As a result, the domain in Keplerian elements is computed only for semi-major axis, eccentricity, and inclination.

2.3.2. *Keplerian elements - ejection velocity relations*

In this section, the equations that relate the variation of the independent Keplerian elements (a, e, i) to the ejection velocity vector $\boldsymbol{\Delta v}$ of Eq. (29) are derived.

The variation in semi-major axis can be computed from the energy equation, as follows.

$$\Delta a(\Delta v, \gamma, \varphi) = \frac{\mu r_P}{2\mu - r_P\left(v_P + \Delta v_m(\Delta v, \gamma, \varphi)\right)^2} - a_P \tag{35}$$

where μ is the planetary constant of the Earth; r_P and v_P are the position and velocity modules of the parent object at the fragmentation epoch; a_P is the semi-major axis of the parent orbit; Δv_m is the variation of the velocity module due to the fragmentation event, defined as follows.

$$\Delta v_m(\Delta v, \gamma, \varphi) = \Big((v_{r_P} + \Delta v\cos\gamma\cos\varphi)^2 + (v_{t_P} + \Delta v\sin\gamma\cos\varphi)^2 + (\Delta v\sin\varphi)^2\Big)^{1/2} - v_P \tag{36}$$

where v_{r_P} and v_{t_P} are the transversal and radial components of the velocity of the parent object at the fragmentation epoch.

The eccentricity vector of a fragment is varied by the ejection velocity vector of Eq. (29), as follows.

$$\boldsymbol{e}_P + \boldsymbol{\Delta e} = \frac{1}{\mu}(\boldsymbol{v}_P + \boldsymbol{\Delta v}) \times (\boldsymbol{h}_P + \boldsymbol{\Delta h}) - \frac{\boldsymbol{r}_P}{r_P} \tag{37}$$

with:

$$(\boldsymbol{h}_P + \boldsymbol{\Delta h}) = \boldsymbol{r}_P \times (\boldsymbol{v}_P + \boldsymbol{\Delta v}) \tag{38}$$

where $\boldsymbol{h}_P$ and $\boldsymbol{\Delta h}$ are the angular momentum of the parent object orbit and its variation due to the fragmentation, respectively, and $\boldsymbol{e}_P$ is the eccentricity vector of the fragmentation orbit. The variation of the eccentricity due to the fragmentation is then computed as:

$$\Delta e\,(\Delta v, \gamma, \varphi) = \|\boldsymbol{e}_P + \boldsymbol{\Delta e}\| - e_P \tag{39}$$

The variation of the inclination Δi is computed as:

$$\Delta i\,(\Delta v, \gamma, \varphi) = \arccos\left(\frac{h_{z_P}^{in.} + \Delta h_z^{in.}}{h_P + \Delta h}\right) - i_P \tag{40}$$

where $h_{z_P}^{in.}$ and $\Delta h_z^{in.}$ are the out-of-plane components of the angular momentum of the parent object orbit and its variation due to the fragmentation in the inertial reference frame, whose sum is computed as follows.

$$h_{z_P}^{in.} + \Delta h_z^{in.} = R_3(\Omega_P)R_1(i_P)R_3(u_P)(\boldsymbol{h}_P + \boldsymbol{\Delta h}) \cdot \widehat{\boldsymbol{k}} \tag{41}$$

where i_P, Ω_P, ω_P and f_P are inclination, right ascension of the ascending node, argument of periapsis and true anomaly of the parent object orbit at fragmentation epoch; $\widehat{\boldsymbol{k}}$ is the unitary vector in the direction of the Z axis of the inertial frame; R_1 and R_3 are the rotation matrices about X and Z axes; $\boldsymbol{h}_P + \boldsymbol{\Delta h}$ is the angular momentum of the orbit of a generic fragment in the RSW reference frame.

Figure 8 shows the variations Δa, Δe, and Δi as function of the in-plane γ and out-of plane φ angles for the same ejection velocity distribution and parent orbit elements considered in Section 2.3.1. Note that the pictures refer to the maximum ejection velocity magnitude $\Delta v = 650$ m/s.

Referring to Figure 8 some considerations can be done:

- The maximum (minimum) of the variation in semi-major axis Δa is always associated to $\gamma = 90$ deg ($\gamma = 270$ deg) and $\varphi = 0$ deg, i.e., when the ejection velocity vector is aligned with (opposite to) the parent velocity vector. In addition, the higher (lower) the kinetic energy of the parent (i.e., the closer to the perigee), the steeper (flatter) the kick in semi-major axis.

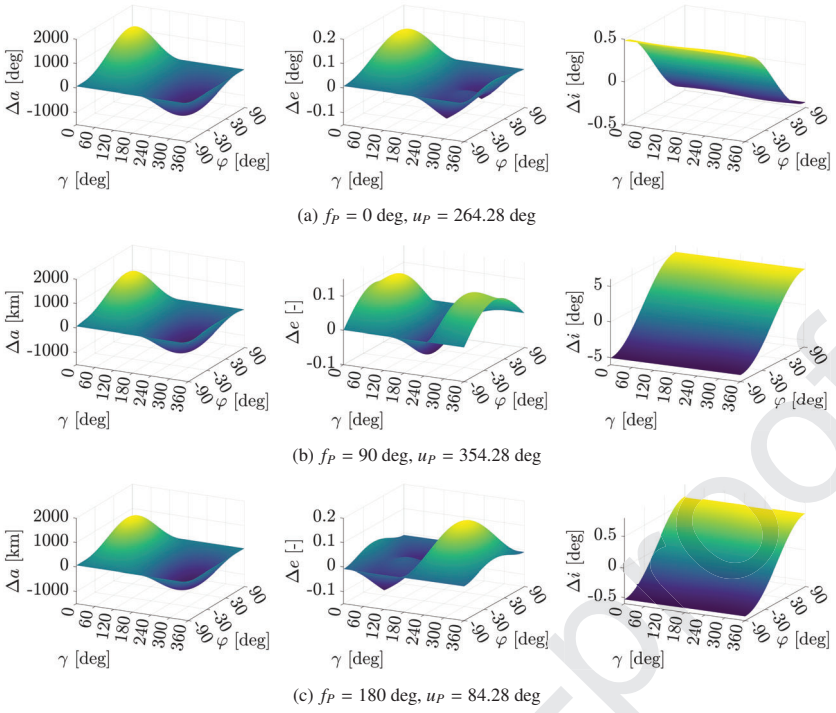

(a) $f_P = 0$ deg, $u_P = 264.28$ deg

(b) $f_P = 90$ deg, $u_P = 354.28$ deg

(c) $f_P = 180$ deg, $u_P = 84.28$ deg

Fig. 8: Variation of semi-major axis, eccentricity and inclination as function of in-plane and out-of-plane ejection velocity angles, for different parent object's true anomaly values.

- The surface of Δe is highly affected by the value of the true anomaly f_p. The cases $f_p = 0$ deg and $f_p = 180$ deg are mirrored, as at perigee a braking manoeuvre is required to circularise the orbit, while at apogee an energy gain is needed. Note that all the surfaces are lower bounded by the minimum of the variation in eccentricity $\Delta e = -e_P$, as eccentricity cannot be negative.

- The variation in inclination Δi is independent of the in-plane angle γ. The maximum (minimum) change is obtained when the latitude is at minimum (maximum), i.e., when the argument of latitude of the parent object u_p is either 0 (90) deg or 180 (270) deg. The orientation of the surface is also affected by the value of u_P; indeed, for $-90 < u_P < 90$ deg positive variations of inclination are obtained for positive out-of-plane angles, while for $90 < u_P < 270$ deg positive variations of inclination follow negative out-of-plane angles.

2.3.3. *Keplerian elements variation due to an isotropic ejection velocity distribution*

The need for a unique domain in Keplerian elements for each ejection velocity limit Δv_j implies that the desired one-to-one correspondence must filter out the dependency on the in-plane γ and out-of-plane φ angles of the ejection velocity vector. The most obvious approach would be to compute the maximum variation of each Keplerian element, given Δv_j; however, this would cause the domain to be unnecessarily vast, covering regions of the phase space with an extremely low value of density. Indeed, it must be understood that the fragments' orbit resulting from the maximisation would be achievable with a single combination of γ and φ, and an ejection velocity magnitude as big as Δv_j. As a result, the associated minimum PDF value $\overline{p}_{\nu,\chi}(\zeta)$ of Eq. (19) would be scaled by a factor $p_\gamma p_\varphi = \cos\varphi/4\pi \leq 1/4\pi$, which means that it would add a negligible contribution to the fragments' distribution. Instead, the domains can be more conveniently computed through:

- Averaging over the in-plane γ and out-of-plane φ ejection velocity angles, according to the PDFs p_γ, p_φ.

- Maximisation over the ejection velocity magnitude Δv_j.

Considering the generic function $g = g(x)$, where the variable x has density p_x, the average value of $g(x)$, $\overline{g}$, over the interval $[x_0, x_1]$ can be computed as:

$$\overline{g} = \frac{1}{F_x(x_1) - F_x(x_0)} \int_{F_x(x_0)}^{F_x(x_1)} g(x)\, \mathrm{d}y \tag{42}$$

where F_x is the CDF of p_x. Recalling that:

$$\mathrm{d}y = p_x\, \mathrm{d}x \tag{43}$$

and performing the change of variables $y \rightarrow x = F_x^{-1}(y)$, the average value $\overline{g}$ can be computed as:

$$\overline{g} = \frac{1}{F_x(x_1) - F_x(x_0)} \int_{x_0}^{x_1} g(x)\, p_x\, \mathrm{d}x \tag{44}$$

If x_0 and x_1 are chosen such that $F_x(x_0) = 0$ and $F_x(x_1) = 1$, then Eq. (44) reduces to:

$$\overline{g} = \int_{x_0}^{x_1} g(x)\, p_x\, \mathrm{d}x \tag{45}$$

For each independent Keplerian element α_i, two boundary values are computed for each area-to-mass ratio bin, diving the domain $\mathcal{D}_{\gamma,\varphi}$ between those angles that lead to positive and negative variations $\Delta\alpha_i$, respectively, as follows.

$$\overline{\Delta\boldsymbol{\alpha}^{+}}_{i}^{(j)}\left(\Delta v_j\right) = \max_{\Delta v \le \Delta v_j} \int_{\gamma_{1_i}^{+}}^{\gamma_{2_i}^{+}} \int_{\varphi_{1_i}^{+}}^{\varphi_{2_i}^{+}} \Delta\alpha_i(\Delta v, \gamma, \varphi)\, p_\gamma p_\varphi \, \mathrm{d}\varphi \mathrm{d}\gamma \tag{46a}$$

$$\overline{\Delta\boldsymbol{\alpha}^{-}}_{i}^{(j)}\left(\Delta v_j\right) = \max_{\Delta v \le \Delta v_j} \int_{\gamma_{1_i}^{-}}^{\gamma_{2_i}^{-}} \int_{\varphi_{1_i}^{-}}^{\varphi_{2_i}^{-}} \Delta\alpha_i(\Delta v, \gamma, \varphi)\, p_\gamma p_\varphi \, \mathrm{d}\varphi \mathrm{d}\gamma \tag{46b}$$

where $\overline{\Delta\alpha^{\pm}}_{i}^{(j)}$ is the maximum (positive or negative) variation of the i^{th} independent Keplerian element α_i subject to an ejection velocity as big as Δv_j, the plus and minus signs indicate the regions in the domain $\mathcal{D}_{\gamma,\varphi}$ that vary positively and negatively the Keplerian element α_i, respectively, and $\Delta\alpha_i = \Delta\alpha_i\left(\Delta v, \gamma, \varphi\right)$ are the variations of semi-major axis, eccentricity or inclinations of Eqs. (35), (39) and (40). It is worth noticing that, as consequence of a fragmentation event, the ejection velocity vector (i.e., some combinations of Δv, γ and φ) of some fragments might be sufficient to inject them on a hyperbolic trajectory with respect to the Earth. If this is the case, the averaging procedure of Eq. (46) becomes meaningless, as it would imply including in the mean also singular cases. In addition, it must be understood that fragments escaping the Earth's gravity field are not relevant for the purpose of analysing the long-term effects of space debris around the Earth, because of their short residence time in the Earth sphere of influence. Therefore, the integrals of Eqs. (46), which are solved through sampling over an equally-spaced grid in γ and φ, are computed excluding those combinations of angles satisfying:

$$\Delta v_m\left(\Delta v, \gamma, \varphi\right) \ge \sqrt{2} v_{circ.} - v_P \tag{47}$$

where $v_{circ.} = \sqrt{\mu / r_P}$ is the velocity magnitude on a circular orbit with radius equal to the fragmentation orbital radius, and Δv_m is the velocity magnitude variation defined in Eq. (36).

Finally, the domains in the subset of Keplerian elements (a, e, i) and area-to-mass ratio A/M are computed as:

$$\mathcal{D}_{\boldsymbol{\alpha}}^{(j)} = \left[\boldsymbol{\alpha}_P + f \cdot \overline{\boldsymbol{\Delta\alpha}^{-}}^{(j)},\ \boldsymbol{\alpha}_P + f \cdot \overline{\boldsymbol{\Delta\alpha}^{+}}^{(j)}\right] \tag{48a}$$

$$\mathcal{D}_{A/M}^{(j)} = 10^{[\chi_{j-1}, \chi_j]} \tag{48b}$$

where f is a safety factor which may enlarge the domain, if needed.

3. Estimation of the initial phase space density distribution

Once the initial domains $\mathcal{D}_{\boldsymbol{\alpha},A/M}^{(j)}$ are defined, the density distribution is estimated through a binning approach. The phase space domain is partitioned into bins and the density is averaged over each bin volume; as a result, the density varies discretely through the domain.

3.1. Gradient-driven phase space discretisation

The accuracy of a binning approach for approximating a general function over a multi-dimensional phase space is inherently linked to its rate of change over a bin volume. The gradient of the probability density function $p_{\nu,\chi}$ with respect to the independent Keplerian elements $\boldsymbol{\alpha}$, $\nabla_{\boldsymbol{\alpha}} p_{\nu,\chi}$, indicates how fast the density is changing locally; thus, it can be used as an indicator of how small the step-size in each Keplerian element $\delta\alpha_i$ should be in order for the discretised distribution to well approximate the actual one. By adopting the derivative chain rule, the gradient of $p_{\nu,\chi}$ with respect to the independent Keplerian elements can be computed as:

$$\nabla_{\boldsymbol{\alpha}} p_{\nu,\chi}(\Delta v, \gamma, \varphi) = p_\chi \nabla_{\boldsymbol{\alpha}} p_{\nu|\chi} = p_\chi \frac{\partial p_{\nu|\chi}}{\partial \nu} \frac{\partial \nu}{\partial \Delta v} \frac{\partial \Delta v}{\partial \boldsymbol{\alpha}} \tag{49}$$

with:

$$\frac{\partial \nu}{\partial \Delta v} = \frac{1}{\Delta v \log 10} \tag{50}$$

and the other partial derivatives computed according to Eqs. (1), (35), (39), and (40).

As an equally-sized binning approach is adopted, the average module of the gradient of the density is chosen as reference for defining the step-sizes in semi-major axis, eccentricity and inclination. Note that, the averaging is carried out over χ, ν, and the ejection velocity angles γ and φ, as follows.

$$\overline{\overline{\overline{\left|\nabla_{\boldsymbol{\alpha}} p_{\nu,\chi}\right|}}} = \frac{1}{\chi_{N_\chi} - \chi_0} \int_{\chi_0}^{\chi_{N_\chi}} p_\chi A(\chi)\, \mathrm{d}\chi \tag{51a}$$

$$A(\chi) = \frac{1}{\overline{\Delta v}(\chi)} \int_0^{\overline{\Delta v}(\chi)} \left|\frac{\partial p_{\nu|\chi}(\nu,\chi)}{\partial \nu}\right| B(\Delta v)\, \mathrm{d}\Delta v \tag{51b}$$

$$B(\Delta v) = \frac{\partial \nu}{\partial \Delta v} \frac{1}{2\pi^2} \int_0^{2\pi} \int_{-\pi/2}^{\pi/2} \left|\frac{\partial \Delta v}{\partial \boldsymbol{\alpha}}\right| \mathrm{d}\varphi\, \mathrm{d}\gamma \tag{51c}$$

The integral over the domain in χ can be written as summation of integrals over the bins in χ. In addition, according to the same assumption done in Section 2.2, the conditional distribution $p_{\nu|\chi}$ is considered independent of χ over a step $\delta\chi_j$. Hence, Eq. (51) can be approximated as:

$$\overline{\overline{\overline{\left|\nabla_{\boldsymbol{\alpha}} p_{\nu,\chi}\right|}}} \approx \frac{1}{\chi_{N_\chi} - \chi_0} \sum_{j=1}^{N_\chi} A\left(\overline{\chi}_j\right) P_\chi\left(\chi_{j-1} < \chi \le \chi_j\right) \tag{52a}$$

$$A\left(\overline{\chi}_j\right) = \frac{1}{\Delta v_j} \int_0^{\Delta v_j} \left|\frac{\partial p_{\nu|\chi}(\nu, \overline{\chi}_j)}{\partial \nu}\right| B(\Delta v)\, \mathrm{d}\Delta v \tag{52b}$$

where the term $A(\chi)$ is evaluated discretely at $\overline{\chi}_j$, which correspond to the centres of the bins in χ, as defined in Eq. (11). Note that, the term $B(\nu)$ is unchanged with respect to Eq. (51). The following heuristic relation between the step-sizes and the derivatives of the density with respect to the Keplerian elements is adopted:

$$\overline{\overline{\overline{\left|\frac{\partial p_{\nu,\chi}}{\partial \boldsymbol{\alpha}_i}\right|}}}\, \delta\boldsymbol{\alpha}_i = \frac{1}{r} \max_{\chi,\nu\, \in\, \mathcal{D}_{\chi,\nu}} p_{\nu,\chi} \tag{53}$$

where r is a factor that can be tuned according to the targeted level of accuracy. The left-hand side of Eq. (53) is the average variation of the density $\overline{\Delta p_{\nu,\chi}}^{(i)}$ associated to a step $\delta\alpha_i$ in

the Keplerian element α_i, which is constrained to be equal to a fraction of the maximum density value. This latter is approximated as follows.

$$\max_{\chi,\nu\,\in\,\mathcal{D}_{\chi,\nu}} p_{\nu,\chi} \approx \max_{j=1,\dots,N_\chi} \overline{p_\chi}^{(j)} p_{\nu|\chi}\left(\nu=\mu_\nu,\overline{\chi}_j\right) = \max_{j=1,\dots,N_\chi} \frac{P_\chi\left(\chi_{j-1}<\chi\leq\chi_j\right)}{\delta\chi_j} p_{\nu|\chi}\left(\nu=\mu_\nu,\overline{\chi}_j\right) \quad (54)$$

where the PDF in χ is averaged over each bin in χ.

3.2. Density averaging through an adaptive Monte Carlo integration

The probability density function in the subset of Keplerian elements (a,e,i) and area-to-mass ratio A/M, $p_{\alpha,A/M}$, can be computed from the probability density function in (χ,ν), $p_{\nu,\chi}$, through change of variables (Frey, 2020; Wittig et al., 2017), as follows.

$$p_{\alpha,A/M} = \frac{p_{\nu,\chi}\left(\psi^{-1}_{\boldsymbol{\nu}\to\boldsymbol{\alpha}}(\boldsymbol{\alpha})\right)}{|\det J_{\boldsymbol{\nu}\to\boldsymbol{\alpha}}|} \quad (55)$$

where $\psi_{\boldsymbol{\nu}\to\boldsymbol{\alpha}}$ is the transformation from velocity vector $\boldsymbol{\nu}=\boldsymbol{\nu}_P+\boldsymbol{\Delta\nu}$ to the subset of Keplerian elements (a,e,i), and $J_{\boldsymbol{\nu}\to\boldsymbol{\alpha}}$ is the Jacobian of the transformation, which can be found in Gonzalo et al. (2021).

Defining $\boldsymbol{x} := (a,e,i,A/M)$ the set of independent phase space variables, the average probability density function $p_{\boldsymbol{x}}$ in the k^{th} bin is computed as:

$$\overline{p_{\boldsymbol{x}}}^{(k)} = \frac{1}{V_{\boldsymbol{x}}^{(k)}} \iiiint_{V_{\boldsymbol{x}}^{(k)}} p_{\boldsymbol{x}}\,\mathrm{d}\boldsymbol{x} \quad (56)$$

The integral of Eq. (56) cannot be solved in close form, thus Monte Carlo integration is adopted. As previously mentioned, the step-sizes for the splitting of the domain are computed according to the average density gradient throughout the phase space; however, the local value of the density gradient is a useful information to determine how fast the density is changing locally. The higher the gradient of the density is, the more samples are needed for accurately computing the average density over the bin volume. Therefore, the number of samples for the Monte Carlo integration is varied according to the local density gradient in the bins. The gradient of the density with respect to the independent phase space variables $\boldsymbol{x}$ can be computed as:

$$\nabla_{\boldsymbol{x}} p_{\nu,\chi} = p_\chi \nabla_{\boldsymbol{x}} p_{\nu|\chi} + p_{\nu|\chi} \nabla_{\boldsymbol{x}} p_\chi \quad (57)$$

Separating $\boldsymbol{x}$ into $\boldsymbol{\alpha}$ and A/M, Eq. (57) can be written as:

$$\nabla_{\boldsymbol{x}} p_{\nu,\chi} = p_\chi \begin{Bmatrix} \nabla_{\boldsymbol{\alpha}} p_{\nu|\chi} \\ \frac{\partial p_{\nu|\chi}}{\partial(A/M)} \end{Bmatrix} + p_{\nu|\chi} \begin{Bmatrix} \mathbf{0}^{3\times1} \\ \frac{\partial p_\chi}{\partial(A/M)} \end{Bmatrix} \quad (58)$$

where $\mathbf{0}^{3\times1}$ is a column vector of three elements equal to zero. The probability density function p_χ, and its derivative, are averaged over the j^{th} bin in χ as follows.

$$p_\chi \approx \overline{p_\chi}^{(j)} = \frac{P_\chi\left(\chi_{j-1}<\chi\leq\chi_j\right)}{\delta\chi_j} \quad (59a)$$

$$\frac{\partial p_\chi}{\partial\chi} \approx \overline{\frac{\partial p_\chi}{\partial\chi}}^{(j)} = \frac{p_\chi\left(\chi_j\right)-p_\chi\left(\chi_{j-1}\right)}{\delta\chi_j} \quad (59b)$$

Finally, the two derivatives with respect to area-to-mass ratio are computed over the j^{th} bin in χ as:

$$\frac{\partial p_{\nu|\chi}}{\partial(A/M)} \approx \frac{\partial p_{\nu|\chi}\left(\nu,\overline{\chi}_j\right)}{\partial\mu_\nu}\frac{\partial\mu_\nu}{\partial\chi}\frac{\partial\chi}{\partial(A/M)} \quad (60a)$$

$$\frac{\partial p_\chi}{\partial(A/M)} \approx \overline{\frac{\partial p_\chi}{\partial\chi}}^{(j)}\frac{\partial\chi}{\partial(A/M)} \quad (60b)$$

with:

$$\frac{\partial\chi}{\partial(A/M)} \approx \frac{1}{\overline{\chi}_j \log 10} \quad (61)$$

Instead, the gradient of the density with respect to the independent Keplerian elements $\boldsymbol{\alpha}$, defined in Eq. (49), is evaluated at some reference points, as the integral average over the bin volume cannot be solved in close form.

The number of samples to be taken is defined according to:

$$N_s = \overline{N_s}\sum_{i=1}^{4}\frac{\Delta p^{(i)}_{\nu,\chi}}{\overline{\Delta p_{\nu,\chi}}^{(i)}} = \overline{N_s}\frac{\delta\boldsymbol{x}_i\cdot\nabla_{\boldsymbol{x}_i}p_{\nu,\chi}}{\frac{4}{r}\max_{\chi,\nu\,\in\,\mathcal{D}_{\chi,\nu}} p_{\nu,\chi}} \quad (62)$$

where $\overline{N_s}$ is a reference number of samples that can be arbitrarily set, depending on the desired level of accuracy. Note that the denominator comes from the constraint imposed in Eq. (53).

The probability density function $p_{\boldsymbol{x}}(\boldsymbol{x})$ defines the probability of finding a single fragment in $\boldsymbol{x}$. Instead, the phase space density, which will be referred to as $n_{\boldsymbol{x}}(\boldsymbol{x})$, describes the number of fragments present in an infinitesimal volume around $\boldsymbol{x}$, i.e.:

$$n_{\boldsymbol{x}}(\boldsymbol{x}) = N p_{\boldsymbol{x}}(\boldsymbol{x}), \qquad \iiiint_{\mathcal{D}_{\boldsymbol{x}}} n_{\boldsymbol{x}}\,\mathrm{d}\boldsymbol{x} = N \quad (63)$$

where N is the number of fragments generated by the fragmentation event, and $\mathcal{D}_{\boldsymbol{x}}$ is the phase space domain occupied by the fragmentation cloud.

It is worth mentioning that the domain $\mathcal{D}_{\alpha,A/M}$ computed in Section 2 is a square one, as the boundaries in semi-major axis, eccentricity and inclination are defined independently from each other. This implies that the edges of the domain are not equally interested by the fragmentation event, which means that the phase space density is not constant along the borders. For instance, on the surfaces at $a = a_P + f\overline{\Delta a^{\pm}}$, it is more likely to find fragments orbiting with an inclination close to the parent one, as all the Δv budget given by Eq. (32) is spent to vary the semi-major axis of the orbit. In addition, not all the regions of the phase space are physically reachable by the ejected fragments. In order for a fragment's orbit to be able to intersect the parent orbit in the fragmentation point, the perigee, r_{per}, and apogee r_{apo}, radii must satisfy:

$$r_{\text{per}} \leq r_P, \qquad r_{\text{apo}} \geq r_P \quad (64)$$

which translate into a boundary curve in the semi-major axis – eccentricity domain, given by:

$$e_i \geq \frac{|a-r_P|}{a} \quad (65)$$

Finally, since the long-term evolution of a fragmentation event is of interest, it is convenient to discard the regions of the phase

space for which the fragments re-enter the atmosphere just after the breakup, i.e.:

$$r_{\text{per}} \leq R_E + h_{\text{atm}} \tag{66}$$

where R_E is the Earth mean radius, and h_{atm} is the altitude limit below which the fragments are assumed to burn in the atmosphere. Also the constraint of Eq. (66) translates into a boundary curve in the (a, e) domain, given by the following inequality:

$$e_r \leq 1 - \frac{R_E + h_{\text{atm}}}{a} \tag{67}$$

In Figure 9 the constraints on intersection and re-entry altitude for the fragmentation of Cosmos-2292 reported in Section 2.3.1 are depicted.

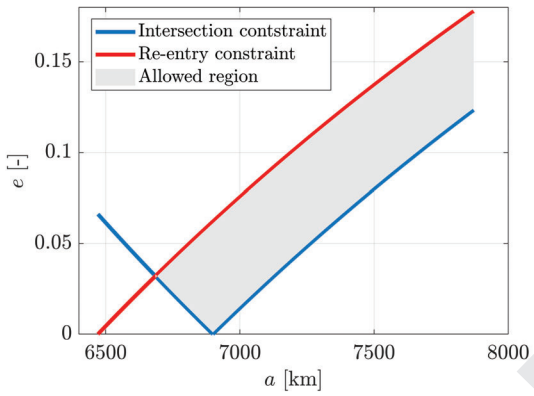

Fig. 9: Intersection and re-entry constraints for a fragmentation in LEO.

Summarising, the phase space density is estimated in the bins satisfying the following three constraints:

1. There exists at least one set of Keplerian elements belonging to the bin such that the perigee is above the re-entry altitude.
2. There exists at least one set of Keplerian elements belonging to the bin, whose related orbit guarantees intersection with the parent orbit in the fragmentation point.
3. The ejection velocity needed to reach the bin's centre satisfies Eq. (32).

3.3. Monte Carlo sampling in non-squared bins

In order for the Monte Carlo integration to be accurate, the samples must be randomly extracted from the bins. This procedure is straightforward when dealing with squared bins, i.e, those that are not crossed by any of the constraints curves of Figure 9. Instead, when either the intersection or re-entry curves cross a bin, the usual routines for extracting random samples over a given range do not apply anymore. To overcome this issue, an inverse transform sampling procedure is performed, based on two PDFs $p_i(a)$ and $p_r(a)$, describing the probability for a sample to be in a region of the bin satisfying the intersection and re-entry constraints, respectively, and having semi-major axis a. Referring to the bins sketched in Figure 10, $p_i(a)$ and $p_r(a)$ can be defined as:

$$p_i(a) = \frac{\mathrm{d}a\left(e_2 - e_i^*(a)\right)}{A_i}, \quad A_i = \delta a\,\delta e - \int_{a_1}^{a_2} e_i^*(a)\,\mathrm{d}a \tag{68a}$$

$$p_r(a) = \frac{\mathrm{d}a\left(e_r^*(a) - e_1\right)}{A_r}, \quad A_r = \int_{a_1}^{a_2} e_r^*(a)\,\mathrm{d}a \tag{68b}$$

where the functions e_i^* and e_r^* are modified with respect to Eqs. (65) and (67), as follows.

$$e_{i/r}^*(a) = \begin{cases} e_{i/r}(a) & \text{if } e_1 < e < e_2 \\ e_1 & \text{if } e \leq e_1 \\ e_2 & \text{if } e \geq e_2 \end{cases} \tag{69}$$

Note that $e_{i/r}$ is the PDF of either the intersection or re-entry constraint.

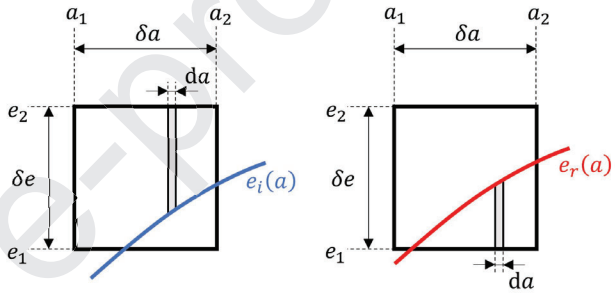

Fig. 10: Bin crossed by intersection and re-entry curves.

The cumulative density functions $F_i(a)$ and $F_r(a)$ can be computed integrating Eqs. (68) over semi-major axis. Finally, the samples are extracted according to the following steps:

1. Extract a random number u from the standard uniform distribution $U(0, 1)$.
2. Compute $\overline{a} = F_{i/r}^{-1}(u)$.

where $F_{i/r}$ is the CDF for either the intersection or re-entry constraint. It is worth noticing that the resulting average density is only representative of the part of the bin satisfying the two constraints. However, the density value is then attributed to the entire bin; hence, it must be scaled according to two factors f_i and f_r, defining the fraction of the bin respecting the intersection and re-entry constraints, respectively. They are easily computed as:

$$f_i = \frac{A_i}{\delta a\,\delta e} \tag{70a}$$

$$f_r = \frac{A_r}{\delta a\,\delta e} \tag{70b}$$

As a result of the estimation of the initial density distribution, each bin belonging to the phase space domain defined in Eq. (48) has an associated density value. Hence, the total number of fragments generated by the fragmentation event can be estimated as:

$$N = \sum_{k=1}^{N_{\text{b}}} V_{\boldsymbol{x}}^{(k)}\,\overline{n_{\boldsymbol{x}}}^{(k)} \tag{71}$$

where N_b is the total number of bins, and $\overline{n_{\boldsymbol{x}}}^{(k)}$ is the average phase space density in the k^{th} bin. Note that the bin volume $V_{\boldsymbol{x}}^{(k)}$ is kept inside the summation because, even though the steps in the subset of Keplerian elements $\boldsymbol{\alpha}$ are constant, the discretisation in A/M can be either equally- or logarithmic-spaced, depending on the way the discretisation in χ is done when numerically solving Eq. (26).

4. Density propagation through the method of characteristics

The phase space density is propagated applying the method of characteristics (MOC) (Jhon et al., 1981) to the continuity equation, here recalled:

$$\frac{\partial n_{\boldsymbol{x}}}{\partial t} + \nabla_{\boldsymbol{y}} \cdot n_{\boldsymbol{x}} \boldsymbol{F} = 0 \tag{72}$$

where t is time, $n_{\boldsymbol{x}}$ the phase space density, $\boldsymbol{y}$ the phase space variables, and $\boldsymbol{F} = \frac{\mathrm{d}\boldsymbol{y}}{\mathrm{d}t}$ the dynamics. The MOC allows transforming the partial differential equation of Eq. (72) into a system of ordinary differential equations, as follows.

$$\begin{cases} \frac{\mathrm{d}\boldsymbol{y}}{\mathrm{d}t} = \boldsymbol{F} \\ \frac{\mathrm{d}n_{\boldsymbol{x}}}{\mathrm{d}t} = -n_{\boldsymbol{x}} \nabla_{\boldsymbol{y}} \cdot \boldsymbol{F} \end{cases} \tag{73}$$

The characteristics are propagated semi-analytically, as a consequence of the averaging of the dynamics equations over the fast angular variable, through the software PlanODyn (Colombo, 2016). It provides the Jacobian of the averaged dynamics with respect to the mean elements for atmospheric drag, J_2 perturbation, solar radiation pressure and luni-solar gravitational perturbations. The characteristics to be propagated are randomly sampled from the density distribution obtained through the procedure explained in Section 3. It is worth noticing that at this stage the density distribution is defined in the four independent variables $\boldsymbol{x}$, which means that it is marginalised over right ascension of the ascending node Ω, argument of perigee ω and true anomaly f. Hence, the sampled characteristics have only four coordinates defined, out of the seven variables in $\boldsymbol{y}$. As explained in Frey & Colombo (2021), for each set (a, e, i) there exist four combinations of Ω, ω, f which guarantee intersection with the parent orbit in the fragmentation point. Calling $\boldsymbol{\beta}$ the set of Keplerian elements (Ω, ω, f), the four solutions of intersection have the following characteristics:

$$\begin{aligned} \boldsymbol{\beta}_1 &= (\Omega_1, \omega_1, f_1) \\ \boldsymbol{\beta}_2 &= (\Omega_1, \omega_2, f_2) \\ \boldsymbol{\beta}_3 &= (\Omega_2, \omega_3, f_1) \\ \boldsymbol{\beta}_4 &= (\Omega_2, \omega_4, f_2) \end{aligned} \tag{74}$$

and satisfy:

$$\begin{aligned} \omega_1 + f_1 &= \omega_2 + f_2 = u_1 \\ \omega_3 + f_1 &= \omega_4 + f_2 = u_2 \\ f_1 &= -f_2 \end{aligned} \tag{75}$$

where u is the argument of latitude. Figure 11 shows the four possible intersections between the Cosmos-2292 orbit, whose elements are reported in Section 2.3.1, and the orbits of potential ejected fragments with semi-major axis a_f and eccentricity e_f equal to the parent ones, and inclination $i_f = 80$ deg. In addition, the ejection velocity magnitude Δv, required to inject the fragments on the intersecting orbits, are reported.

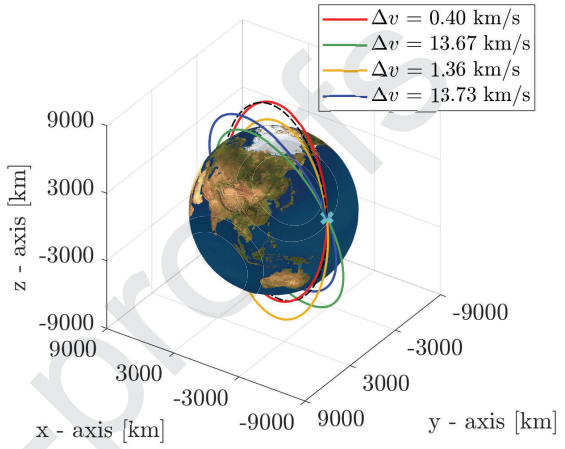

Fig. 11: Four possible intersections between parent orbit and fragments' orbit.

By imposing the intersection, the 4D density distribution in $\boldsymbol{x}$, $n_{\boldsymbol{x}}(\boldsymbol{x})$, is unfolded into a 7D distribution in $\boldsymbol{y}$, $n_{\boldsymbol{x}}(\boldsymbol{y})$. Note that, despite of the different phase space upon which the density is defined, its value still corresponds to the number of fragments per unit semi-major axis, eccentricity, inclination and area-to-mass ratio. The relation between the folded $n_{\boldsymbol{x}}(\boldsymbol{x})$ and unfolded $n_{\boldsymbol{x}}(\boldsymbol{y}) \equiv n_{\boldsymbol{x}}(\boldsymbol{x}, \boldsymbol{\beta})$ distributions is provided by the following equation:

$$n_{\boldsymbol{x}}(\boldsymbol{x}) = \sum_{j=1}^{4} w_j \iiint_{\mathbb{R}^3} n_{\boldsymbol{x}}(\boldsymbol{x}, \boldsymbol{\beta}) \, \delta\left(\boldsymbol{\beta} - \overline{\boldsymbol{\beta}}_j(\boldsymbol{\alpha})\right) \mathrm{d}\boldsymbol{\beta} \tag{76}$$

where $\delta(\cdot)$ is the Dirac delta function, $\overline{\boldsymbol{\beta}}_j$ is one of the combinations of (Ω, ω, f) reported in Eq. (74), and w_j is a weight that scales the density value of each intersecting orbit, depending on the needed ejection velocity.

Under the effect of orbital perturbations, the orbit of some fragmentation debris might evolve such that the perigee reaches an altitude, at which it can be assumed that the thermal stress exerted by the atmosphere causes those fragments to burn. In this work, the limit altitude h_{atm} is assumed at 100 km. If a piece-by-piece propagation method or, in general, if the distribution of the sampled characteristics in the phase space resembles the phase space density (i.e., more characteristics are sampled in the high-density regions), the number of fragments at time t can be approximated as:

$$N(t) \approx N(t_0) \frac{N_c(t)}{N_c(t_0)} \tag{77}$$

where N_c is the number of survived characteristics. Instead, in this work, the sampled characteristics are uniformly distributed

in the phase space, which means that the number of survived characteristics over time would represent the evolution of a fragments' cloud, whose density is described by a uniform distribution. To estimate the number of survived fragments with phase space density $n_{\boldsymbol{x}}(\boldsymbol{x})$, the following relation is adopted:

$$N(t) = N(t_0)\frac{\sum_{k=1}^{N_c(t)} \overline{n_{\boldsymbol{x}}}^{(k)}(t_0)}{\sum_{k=1}^{N_c(t_0)} \overline{n_{\boldsymbol{x}}}^{(k)}(t_0)} \tag{78}$$

which weights the re-entered characteristics based on the associated density value at fragmentation epoch. Note that it is mandatory to refer to the fragmentation epoch to avoid a potential unfeasible estimated evolution of the number of fragments over time. Indeed, the integration of the density equation of Eq. (72) might lead to both positive and negative variation of the density over time; hence, referring to a reference epoch different from the initial one t_0 may potentially induce an increase of the number of fragments over time, which is physically impossible.

5. Density interpolation through binning

With the method of characteristics, a partial differential equation is transformed into an ordinary differential equation along the characteristic curves (Jhon et al., 1981). This means that the solution of the continuity equation is known only on the characteristic curves, at any time. Propagating a population of samples allows to picture the dynamical evolution of the fragments' cloud; nevertheless, characteristics propagated to the same epoch form a scattered point cloud in the phase space, which must be interpolated to retrieve a density distribution in the entire domain. Here, the propagated samples are interpolated through binning in a (up to) 6D phase space of slow-varying orbital elements $(a, e, i, \Omega, \omega)$ and area-to-mass ratio A/M, attributing a density value to each bin, based on the density values of the characteristics in it. Note that the fast angular variable is not accounted in the interpolation because, as motivated in Jehn (1990), the fragments' cloud can be assumed to be randomised in mean anomaly M after few orbital periods, after which the debris form a toroid around the Earth. Indeed, note that the objective of this work is to monitor the long-term evolution of clouds of fragments, which implies propagation times much longer than the time needed for the toroid formation.

The uniform distribution of the samples over the phase space allows to consider the initial characteristics as representative of the entire fragments' cloud, which strictly applies only if at least one sample is extracted from each bin in the phase space domain. Under this condition the following equality is satisfied:

$$N(t_0) = \sum_{k=1}^{N_b} V_{\boldsymbol{x}}^{(k)}\, \overline{n_{\boldsymbol{x}}}^{(k)}(t_0) = \sum_{k=1}^{N_c(t_0)} V_{\boldsymbol{x}}^{(k)}\, \overline{n_{\boldsymbol{x}}}^{(k)}(t_0) \tag{79}$$

Hence, each characteristic can be considered as representing a number of fragments as high as $N^{(k)}(t) = V_{\boldsymbol{x}}^{(k)}\, \overline{n_{\boldsymbol{x}}}^{(k)}(t)$. This implies that the interpolation through binning can be done summing the contribution of all the characteristics that share the same bin, i.e.:

$$\overline{n_{\boldsymbol{x}}}^{(k)}(t) = \sum_{j=1}^{N_c^{(k)}(t)} n_{\boldsymbol{x}_j}^{(k)}(t) \tag{80}$$

where $n_{\boldsymbol{x}_j}^{(k)}$ is the density value of the j^{th} sample moving in the k^{th} bin at time t. Note that the density values are eventually scaled by a factor f_s computed according to Eq. (81), that constrains the integral of the density over the phase space domain to coincide with the total number of fragments, at any time.

$$f_s = \frac{N(t)}{\sum_{k=1}^{N_b} V^{(k)} \overline{n_{\boldsymbol{x}}}^{(k)}(t)} \tag{81}$$

with $N(t)$ defined in Eq. (78).

Depending on the number of propagated samples and dimension of the step-sizes used, parts of the interpolated density distributions may have holes or discontinuities, not because of the actual dynamical evolution of the cloud, but due to lack of information (i.e., samples) in some regions of the phase space. The most straightforward, but not efficient, way to overcome this issue is to increase the number of propagated samples, with a consequent rise of the computational cost. Instead, in this work, the problem is addressed during the interpolation process. The propagation of a sample on its characteristic curve allows retrieving the history of the density distribution inside a multi-dimensional stream-tube, whose section, at any time t, is characterised by an infinitesimal volume $\mathrm{d}\boldsymbol{x}$. This means that, in theory, an infinite number of characteristics should be propagated to get the phase space density at any point in space and time. Having a finite number of samples evenly distributed over the domain $\mathcal{D}_{\boldsymbol{x}}$ and separated, on average, by a distance $\|\delta\boldsymbol{x}\|$ at fragmentation epoch, it can be assumed that each characteristic is representative of a finite volume $V_{\boldsymbol{x}}^{(k)}$ built around the sample. Under the assumption that the variation over time of the finite volume is negligible, i.e. $V_{\boldsymbol{x}}^{(k)}(t) \approx V_{\boldsymbol{x}}^{(k)}(t_0)$, it can be assumed that each characteristic represents $N^{(k)}(t)$ fragments uniformly distributed in a cuboid-like bin moving in space and time. Therefore, at each time epoch at which the density distribution is retrieved, the density of each propagated sample is divided among all the bins of the interpolation grid that intersect the hypothetical cuboid around the characteristic, on the basis of the shared area. Note that this process is integral preserving.

The use of a binning approach in a six-dimensional phase space is challenging from a memory usage standpoint. However, in most of the cases, the debris generated by a fragmentation event remain bounded is certain regions of the phase space. Therefore, the data storage technique for sparse distributions explained in Colombo et al. (2021) is here adopted.

6. Application of the model to the fragmentation of Ariane 5 in GTO

The continuum formulation presented in this paper is applied to the modelling of the cloud of fragments generated by the potential explosion of an Ariane 5 rocket body in Geostationary Transfer Orbit (GTO). The objective of this section is to assess

the accuracy of the approach, by comparing some relevant results against a Monte Carlo simulation. The analysis here proposed considers fragments in the range 1 cm - 1 m, and propagates the generated debris cloud for a period of 15 years under atmospheric drag, J_2 perturbation, SRP, and luni-solar perturbations through the PlanODyn propagator (Colombo, 2016). The considered fragmentation Keplerian elements are reported in Table 3. They correspond to the osculating elements of the Ariane 5 rocket body with NORAD ID 26110 on the 06/04/2022. Note that the fragmentation mass is set to 1190 kg. According to the NASA SBM, the number of objects generated by an explosion depends on the parameter S (Johnson et al., 2001), which, as motivated in Krisko (2011), can vary between 0.1 and 1 according to the fragmentation type. Following the same approach proposed in Letizia et al. (2018), the parameter S is set according to the following relations:

$$S = \begin{cases} k\frac{M_p\ [\mathrm{kg}]}{10000\ [\mathrm{kg}]} & \text{if } kM_p < 10000 \text{ kg} \\ 1 & \text{if } kM_p \geq 10000 \text{ kg} \end{cases} \tag{82}$$

with $k = 1$ for payloads and $k = 9$ for rocket bodies. As a result, the parameter S for the proposed application is set to 1.

Table 3: Ariane 5 fragmentation Keplerian elements.

a [km]	e [-]	i [deg]	Ω [deg]	ω [deg]	f [deg]
24443	0.709	6.54	253.22	271.81	43.56

6.1. Density distribution at fragmentation epoch

The initial phase space density distribution is estimated considering 20 equally-spaced bins in area-to-mass ratio. The parameter ζ of Eq. (24) is set to 0.95, which implies that the model is expected to describe 95% of the fragments' cloud. For the discretisation of the domain in Keplerian elements, the parameter r of Eq. (53), which tunes the average step in the PFD $p_{\nu,\chi}$ across a bin, is constrained to $r = 10$. This means that, on average, over a step $\delta\alpha_i$ in the Keplerian element α_i the PDF $p_{\nu,\chi}$ undergoes a variation equal to the 10% of the maximum density value over the domain $\mathcal{D}_{\chi,\nu}$. The resulting step-sizes in the independent Keplerian elements $\boldsymbol{\alpha}$, computed according to Eq. (53), are reported in Table 4.

Table 4: Step-sizes in the independent Keplerian elements $\boldsymbol{\alpha}$ for the estimation of the intial phase space density distribution.

δa [km]	δe [-]	δi [deg]
514.4	0.00571	0.133

To prove the importance of an automatised tool for setting the step-sizes for the grid in Keplerian elements, the average density gradient with respect to the independent Keplerian elements of Eq. (51), and the resulting step-sizes $\delta\boldsymbol{\alpha}$, are computed for $N = 72$ initial argument of latitude u_p of the parent object. The resulting profiles of the averaged partials (blue lines) and step-sizes (red lines) are reported in Figure 12. Note that for generating the plots, the argument of periapsis ω_p is set to zero, while the true anomaly f_p is varied from 0 to 360 deg.

As it can be observed, the fragmentation location along the orbit strongly affects how the fragments distribute over the phase space. As already motivated in Section 2.3.2, the higher the kinetic energy is (i.e., the closer to the periaspsis), the more widely the fragments spread over semi-major axis. Indeed, the average partial derivative with respect to semi-major axis (step δa) has a minimum (maximum) at $f_p = 0$ deg. The step-size in eccentricity has two maxima at perigee and apogee and two minima when the true anomaly is either 120 deg or 240 deg. Finally, the partial derivative with respect to inclination has two thin, high peaks for $u_p = 90$ or 270 deg, because, as explained in Section 2.3.2, the farther the fragmentation occurs from the equatorial plane, the narrower the fragments are distributed over inclination. As it can be further noticed, when the fragmentation occurs at the apogee of the parent orbit, the explosion affects the most the fragments inclination, as the velocity magnitude is at minimum and, thus, the velocity vector can be rotated more easily to change the inclination.

In Figure 13 the initial density distribution in the subset of the independent variables $\boldsymbol{x}$ is depicted. As already highlighted in Section 3.2, the fragments are bounded by the constraints on intersection with the parent object and re-entry altitude. As a result, in the semi-major axis - eccentricity domain, the fragments occupy the small portion of the phase space between the two curves of Eqs. (65) and (67). Instead, by looking at the distributions in area-to-mass ratio, it can be appreciated how the density reaches the same minimum density value at different value of the Keplerian elements $\boldsymbol{\alpha}$ (i.e., different ejection velocities) for each area-to-mass ratio bin. This result allows to graphically interpret the equality constraints of Eq. (20), where it was asked to solve for the ejection velocity limits ν_j to guarantee the same density value at the edges of the distribution.

6.2. Cloud propagation

From the density distribution of Figure 13, one characteristic is randomly sampled from each bin. By imposing intersection with the parent orbit in the fragmentation point, the samples are expanded in the full set of 7 coordinates. Among the expanded characteristics, only those with a density $n_{\boldsymbol{x}}(\boldsymbol{y}) > n_{\min}$ are propagated, with $n_{\min}$ computed as:

$$\sum_{k\,:\,n_{\boldsymbol{x}}^{(k)} > n_{\min}} n_{\boldsymbol{x}}^{(k)}\, V_{\boldsymbol{x}}^{(k)} = 0.99 \cdot N \tag{83}$$

where N is the estimated total number of fragments, reported in Eq. (71). Indeed, it must be understood that the domain boundaries are defined in the subset of Keplerian elements $\boldsymbol{\alpha}$ and, as detailed in Section 4, for each $\boldsymbol{\alpha}$ there exist 4 sets of dependent Keplerian elements $\boldsymbol{\beta}$, characterised by a different density value, according to Eq. (76). Note that, depending on the parent orbit, the difference might be of several order of magnitude. The sampling procedure resulted in 27040 characteristics to be propagated. The density distribution is retrieved every 30 days through the interpolation procedure explained in Section 5. Figure 14 shows the density distributions in the slow-varying Keplerian elements, at fragmentation epoch and 5, 10, and 15 years after fragmentation.

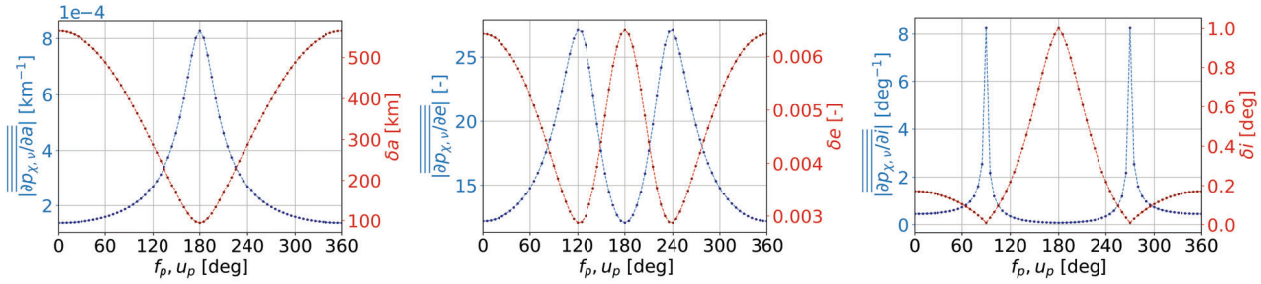

(a) Semi-major axis (b) Eccentricity (c) Inclination

Fig. 12: Average partial derivatives of the PDF $p_{\nu,\chi}$ with respect to the independent Keplerian elements $\boldsymbol{\alpha}$ and resulting step-sizes $\delta\alpha_i$.

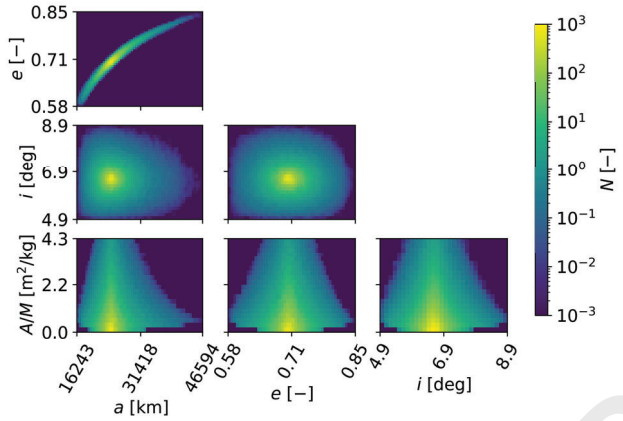

Fig. 13: Phase space density distribution in the subset of the independent variables $\boldsymbol{x}$, at fragmentation epoch.

By looking at Figure 14 the following considerations can be done:

- Under the effect of atmospheric drag, the fragments characterised by a sufficiently small perigee radius undergo a circularisation of the orbit.
- SRP and luni-solar perturbations induce notable variations in the orbits' inclination over time. In addition, they cause a bifurcation in the semi-major axis - eccentricity domain, happening approximately at $a = 14000$ km and $e = 0.5$.
- The distribution in right ascension of the ascending node Ω and argument of periapsis ω domain remains confined on two thin diagonal lines. This is in contrast with the typical behaviour of a LEO fragmentation, where each combination of Ω, ω is approximately characterised by the same density value, which allows to get rid of the these variables, except for the very first stage of the cloud evolution. The different behaviour is due to the high eccentricity of the considered orbit, which causes the fragments to gather in a small range of values in ω, differently from the quasi-circular orbits of the LEO region. The angular coefficient $m_{(\Omega,\omega)}$ of the resulting line-like distribution is approximately given by the arc-tangent of the ratio between the long-term rates of change $\dot{\Omega}_{J_2}$ and $\dot{\omega}_{J_2}$ induced by the J_2 perturbation, here recalled (Vallado & McClain, 2007):

$$\dot{\Omega}_{J_2} = -W\frac{\cos i}{(1-e^2)^2} \tag{84a}$$

$$\dot{\omega}_{J_2} = W\frac{5\cos^2 i - 1}{2(1-e^2)^2} \tag{84b}$$

with W oblateness parameter. The resulting angular coefficient is:

$$m_{(\Omega,\omega)} = \arctan\left(-\frac{5\cos^2 i - 1}{2\cos i}\right) \approx -63.4 \text{ deg} \tag{85}$$

6.3. Accuracy analysis against Monte Carlo simulation

To validate the continuum formulation presented in this paper, a Monte Carlo simulation is performed. It involves 20 separate clouds' propagations; for each of them, the NASA SBM is used for generating the population of ejected fragments, whose coordinates are propagated under the same force model considered in Section 6.2, for a total of 189925 propagated characteristics (the number corresponds to 20 times the average number of generated fragments, according to the NASA SBM). Note that this number is probably not sufficiently high for a Monte Carlo simulation, in particular for well-characterising the low-density regions, where only few characteristics are sampled. However, this choice was constrained by the massive computational time required for propagating the huge population of samples under the relatively complex dynamical model considered. The fragments distributions are retrieved through binning at the same time epochs, counting the fragments belonging to the same bin. The results of the 20 simulations are eventually summed up. In Figure 15, the continuum approach and the Monte Carlo simulation are compared in terms of the number of survived fragments N (i.e., those that did not re-entered the atmosphere) over time. The percentage relative error between the methods is also displayed. It is computed as:

$$\text{Err.}_{\%}(t) = \frac{N_{\text{MC}}(t) - N_{\text{CA}}(t)}{N_{\text{MC}}(t)} \cdot 100 \tag{86}$$

with N_{MC} and N_{CA} number of in-orbit fragments estimated by the Monte Carlo simulation and continuum approach method, respectively.

As it can be observed, the continuum approach captures approximately 94.1% of the cloud at fragmentation epoch, which

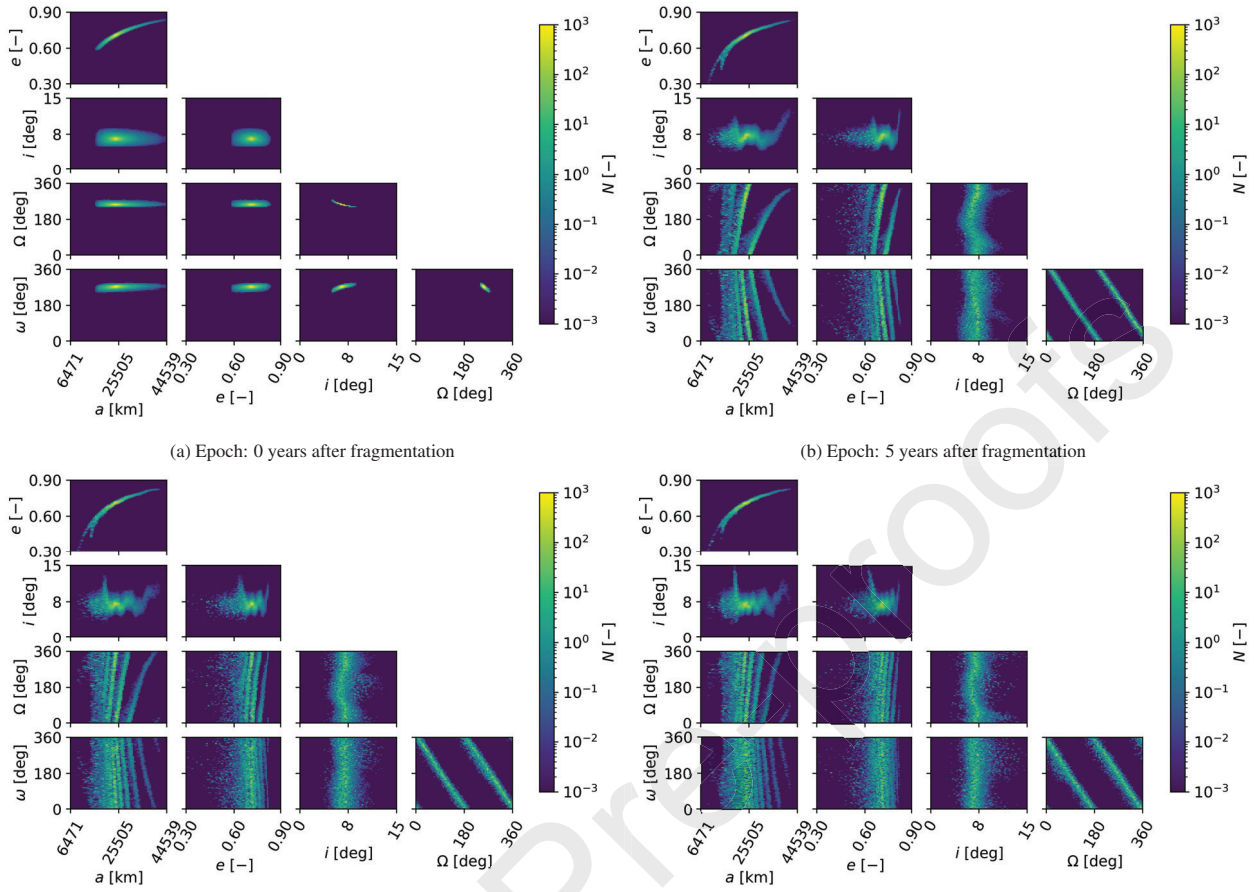

(a) Epoch: 0 years after fragmentation

(b) Epoch: 5 years after fragmentation

(c) Epoch: 10 years after fragmentation

(d) Epoch: 15 years after fragmentation

Fig. 14: Phase space density distribution in the slow-varying Keplerian elements over time.

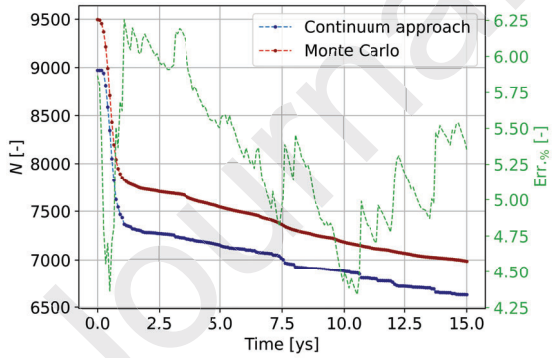

Fig. 15: Number of in-orbit fragments over time, comparison between continuum formulation and Monte Carlo simulation.

is expected because of the constraint on ζ and the pruning of the low-density characteristics according to Eq. (83). In addition, over the 15 years of propagation, the percentage relative error oscillates between the 4.25% and the 6.25%, and it does not follow a monotonic trend over time. Therefore, the model is expected to be valid even for longer propagation times. As it can further appreciated, for the Monte Carlo simulation the number of survived fragments smoothly varies over time; on the contrary, some sudden variations are estimated by the continuum formulation. The different behaviour is explained by the different philosophy of the two approaches. The Monte Carlo simulation accounts for a series of piece-by-piece propagations, where the number of fragments burned in the atmosphere varies continuously once the coordinates of the samples are such that the orbits cross the established re-entry altitude. On the other hand, in the continuum approach, when a characteristic falls in the atmosphere, the number of lost fragments is weighted by the density associated to the characteristic. As a result, when a sample with a high density re-enters, an instantaneous decrease of the number of in-orbit fragments is experienced.

The comparison on the number of in-orbit fragments over time is not sufficient to demonstrate the validity of the model. It is also necessary that the phase space density distribution estimated by the continuum formulation resembles the fragments distribution of the Monte Carlo simulation. In other words, by placing a control volume in different regions of the phase space, the number of hosted fragments measured by the two methods must be comparable. Considering that the right ascension of the ascending node Ω and argument of periapsis ω are rapidly changing, monitoring a fixed area in the 5 slow-varying Keplerian elements would result in a profile where most of the time a null flux of fragments is experienced. Therefore, the comparison is here performed after having marginalised the density

distribution over Ω and ω. A set of five coordinates in the independent variables $\boldsymbol{\alpha}$ are monitored, located in different regions of the phase space. The choice is also density-driven: points P_1 and P_2 are located in a low-density region, P_3 and P_4 in medium-density region, while P_5 is placed in correspondence of the density peak at fragmentation epoch. Note that, in order for the comparison to be statistically valid, a sufficiently high number of fragments must cross the control volume over time; hence, the very low-density regions are not considered in the analysis. The set of five chosen coordinates is listed in Table 5, and displayed above the density distribution in Figure 16.

Table 5: List of coordinates for the comparison with the Monte Carlo simulation.

	a [km]	e [-]	i [deg]
P_1	20617	0.656	7.01
P_2	29363	0.757	6.34
P_3	23189	0.694	5.94
P_4	26276	0.729	7.54
P_5	24218	0.706	6.61

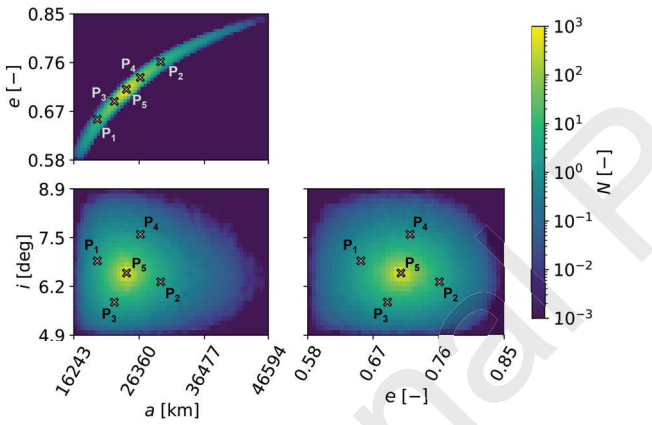

Fig. 16: Location of the coordinates for the comparison with the Monte Carlo simulation above the initial density distribution in the independent Keplerian elements $\boldsymbol{\alpha}$.

The dimensions of the control volume considered are the following: $\Delta a = 500$ km, $\Delta e = 0.01$, $\Delta i = 0.5$ deg. Note that the control volume is set sufficiently big on purpose; indeed, it is worth recalling that the model here proposed aims to estimate the evolution of a cloud of fragments from a probabilistic perspective, within a feasible computational time. The random sampling of the characteristics from the initial bins' population implies that the resulting cloud evolution is not expected to coincide on the small scale. Instead, what is reasonable to ask, is a similar estimation of the cloud evolution on the medium scale, both in space and time. Requiring a high accuracy on the very small scale would imply increasing considerably the resolution of the initial density distribution (i.e., very small step-sizes $\delta\boldsymbol{\alpha}$), which would translate into a massive population of characteristics to be propagated.

Figure 18 depicts the profiles of the number of fragments hosted by the five control volumes over time, measured by the continuum approach and the Monte Carlo simulation. Note that, on top of each plot, the average percentage relative error between the two simulations is displayed. It is computed as:

$$\overline{\text{Err.}_{\%}} = \frac{1}{N_t} \sum_{j=1}^{N_t} \frac{\left| N_{\text{MC}}^{(j)} - N_{\text{CA}}^{(j)} \right|}{\max\left(N_{\text{MC}}^{(j)}, 1 \right)} \tag{87}$$

where $N_{\text{MC}}^{(j)}$ and $N_{\text{CA}}^{(j)}$ are the number of fragments in the control volume at the j^{th} time epoch estimated by the Monte Carlo simulation and continuum approach, respectively, and N_t is the number of time epochs considered. Figure 17, instead, represents the cumulative number of fragments over time. In this case, the percentage relative error at the end of the propagation is shown.

As it can be observed, the results of the two approaches are similar in most of the cases; in particular, the two profiles follow the same behaviour, which is characterised by considerable oscillations, for all the control volumes except for the one placed in P_1, where the curves start diverging 5 years after fragmentation. Note that, as already mentioned, this behaviour might be caused by a not sufficiently high number of propagations performed in the Monte Carlo simulation. As a result, the estimated fragments' distribution in the low-density regions may lack of accuracy. On the other hand, in correspondence of the peaks, the profiles show some relevant differences in terms of magnitude. However, the error in the estimated cumulative number of fragments over time is less than 20% for all the cases. Determining the effect of this inaccuracy is a hard task and depends on the way its impact is assessed. In future works, the results of the cloud propagation model will be provided as input to a density-based collision risk method to compute the effect of a fragmentation on a given target satellite. In that framework, the error introduced by the model will be assessed in terms of estimated collision probability. So far, the reported percentage error is adopted just as an indicator of the model accuracy, and the results obtained are considered to satisfy the objective of the proposed method, which aims at finding a compromise between accuracy and computational efficiency.

7. Conclusions

The impact with centimetre or sub-centimetre fragments, moving at a relative speed as high as 10 km/s, proved to be sufficient to cause serious damages on active satellites. When reducing to such a small size for the debris, the deterministic approaches, as Monte Carlo simulations, demonstrated not to be viable, due to the massive computational cost required. As a result, continuum formulations, which treat the space debris as a cloud, has been investigated, most of the times under simplified force models.

This paper aimed at extending the continuum approach to any non-linear dynamics, which would guarantee the applicability to any orbital region. Therefore, combined to the MOC, a binning approach was used to interpolate the propagated characteristics at some specified time epochs, as it is supposed to

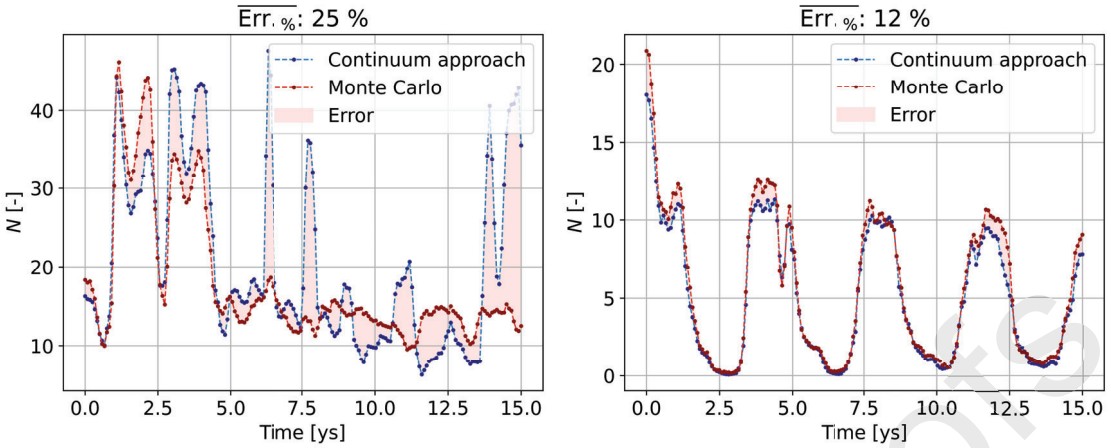

(a) Control volume P_1

(b) Control volume P_2

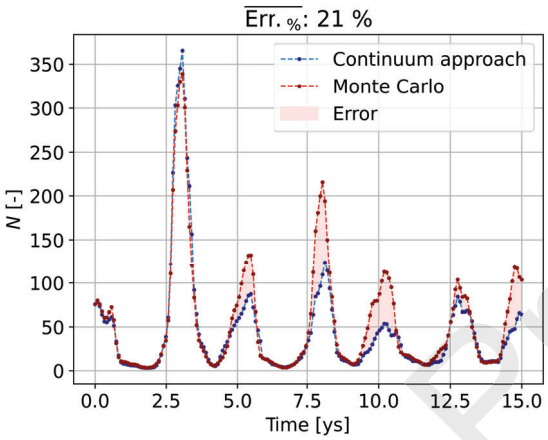

(c) Control volume P_3

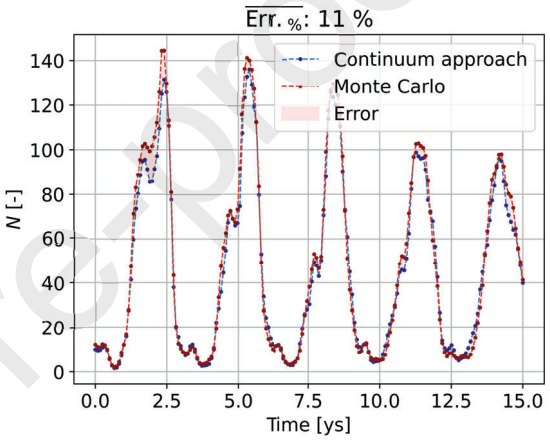

(d) Control volume P_4

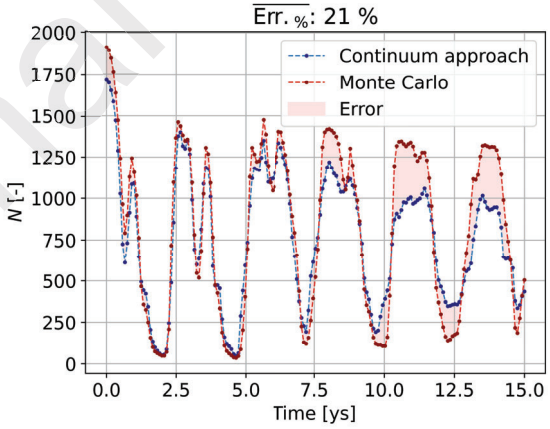

(e) Control volume P_5

Fig. 17: Number of fragments hosted by the control volumes with middle point defined in Table 5.

be agnostic to the dynamical regime considered. The potential issue related to the use of a binning approach in a multi-dimensional phase space was addressed through probabilistic models that dramatically limited the computational effort. Firstly, the semi-analytical model for determining the boundaries in ejection velocity and area-to-mass ratio, which were then transformed into a series of domains in Keplerian elements and area-to-mass ratio, allowed to accurately target the regions of the phase space which are more likely to host the ejected fragments. The gradient-driven discretisation of the phase space, as well as the adaptive Monte Carlo integration, provided an automatised estimation of the fragments' density, which can be applied to any fragmentation type and orbit. The comparison against a Monte Carlo simulation on the poten-

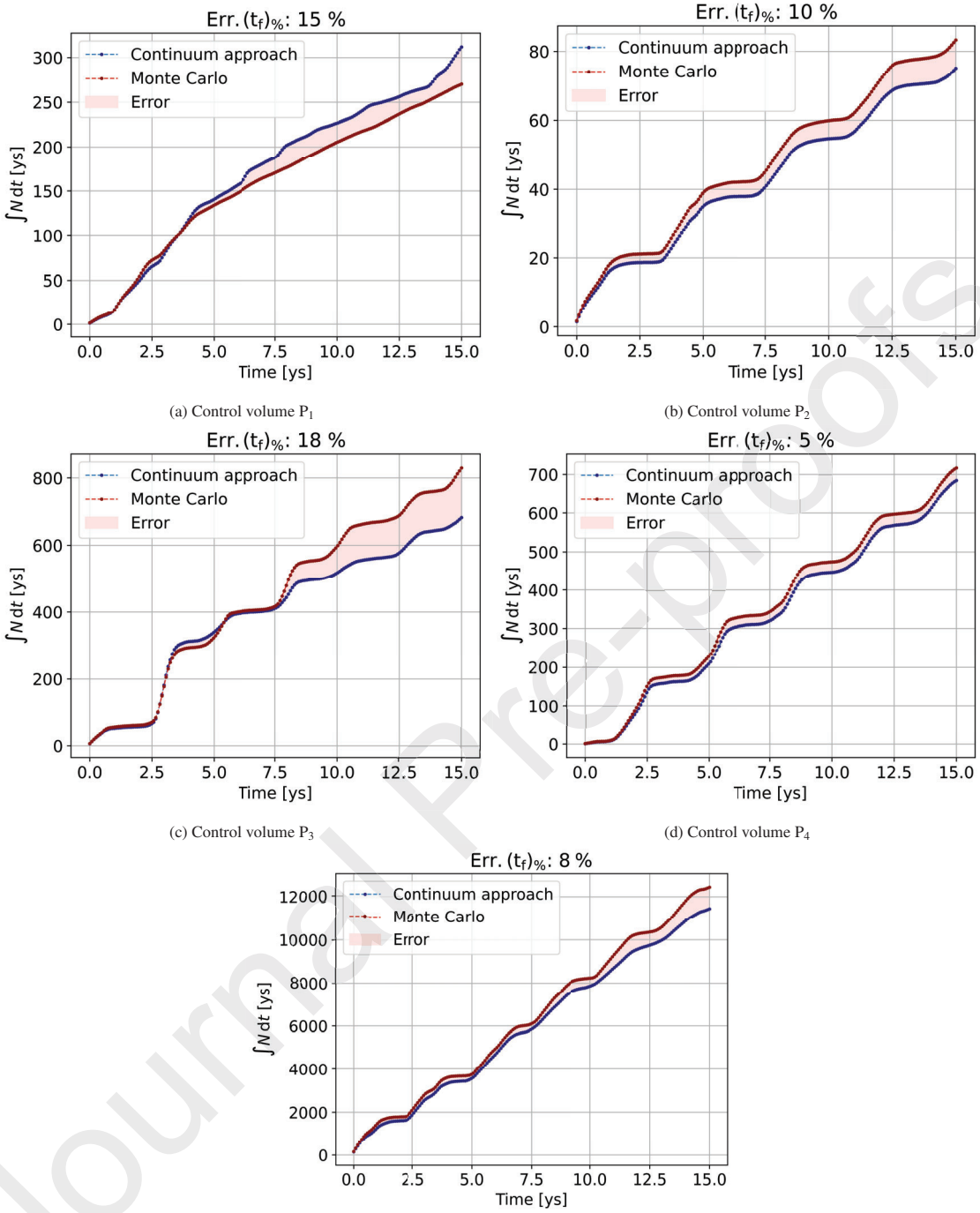

(a) Control volume P_1

(b) Control volume P_2

(c) Control volume P_3

(d) Control volume P_4

(e) Control volume P_5

Fig. 18: Cumulative number of fragments hosted by the control volumes with middle point defined in Table 5.

tial fragmentation of an Ariane 5 rocket body in GTO gave promising results. Indeed, even though some differences were registered, the model proved to be sufficiently accurate on the medium scale.

8. Acknowledgments

This project has received funding from the European Research Council (ERC) under the European Union's Horizon 2020 research and innovation programme (grant agreement No 679086 - COMPASS) and from the European Space Agency contract 4000133981/21/D/KS.

References

Adushkin, V., Aksenov, O., Veniaminov, S. et al. (2020). The small orbital debris population and its impact on space activities and ecological safety. *Acta Astronautica*, *176*, 591–597. doi:10.1016/j.actaastro.2020.01.015.

Ashenberg, J. (1994). Formulas for the phase characteristics in the problem of low-earth-orbital debris. *Journal of Spacecraft and Rockets*, *31*(6), 1044–1049. doi:10.2514/3.26556.

Barrows, S. P., Swinerd, G. G., & Crowther, R. (1996). Review of debris-cloud modeling techniques. *Journal of Spacecraft and Rockets*, *33*(4), 550–555. doi:10.2514/3.26798.

Chobotov, V. A. (1990). Dynamics of orbiting debris clouds and the resulting collision hazard to spacecraft. *Journal of the British Interplanetary Society*, *43*, 187–194.

Colombo, C. (2016). Planetary orbital dynamics (planodyn) suite for long term propagation in perturbed environment. In *Proc. of the 6th International Conference on Astrodynamics Tools and Techniques*.

Colombo, C., Trisolini, M., Gómez, J. L. G. et al. (2021). Design of a software to assess the impact of a space mission on the space environment. In *Proc. of the 8th European Conference on Space Debris*.

Drolshagen, G. (2008). Impact effects from small size meteoroids and space debris. *Advances in Space Research*, *41*, 1123–1131. doi:10.1016/j.asr.2007.09.007.

ESA Space Debris Office (2021). *ESA's annual space environment report*. Technical Report.

Frey, S. (2020). *Evolution and hazard analysis of orbital fragmentation continua*. Ph.D. thesis Politecnico di Milano.

Frey, S., & Colombo, C. (2021). Transformation of satellite breakup distribution for probabilistic orbital collision hazard analysis. *Journal of Guidance, Control, and Dynamics*, *44*(1), 88–105. doi:10.2514/1.G004939.

Frey, S., Colombo, C., & Lemmens, S. (2019). Application of density-based propagation to fragment clouds using the starling suite. In *Proc. of the First International Orbital Debris Conference*.

Gonzalo, J. L., Colombo, C., & Di Lizia, P. (2021). Analytical framework for space debris collision avoidance maneuver design. *Journal of Guidance, Control, and Dynamics*, *44*(3), 469–487. doi:10.2514/1.G005398.

Jehn, R. (1990). Dispersion of debris cloud from in-orbit fragmentation events. *ESA Journal*, *15*(1), 63–77.

Jhon, F., LaSalle, J. P., & Sirovich, L. (1981). *Partial Differential Equations*. (4th ed.). New York: Springer.

Johnson, N. L., Krisko, P., Liou, J.-C. et al. (2001). Nasa's new breakup model of evolve 4.0. *Advances in Space Research*, *28*(9), 1377–1384. doi:10.1016/S0273-1177(01)00423-9.

Krag, H., Serrano, M., Braun, V. et al. (2017). A 1 cm space debris impact onto the sentinel-1a solar array. *Acta Astronautica*, *137*, 434–443. doi:10.1016/j.actaastro.2017.05.010.

Krisko, P. H. (2011). Proper implementation of the 1998 nasa breakup model. *Orbital Debris Q. News*, *15*, 4–5.

Letizia, F. (2018). Extension of the density approach for debris cloud propagation. *Journal of Guidance, Control, and Dynamics*, *41*(12), 2651–2657. doi:10.2514/1.G003675.

Letizia, F., Colombo, C., & Lewis, H. (2015a). 2d continuity equation method for space debris cloud collision analysis. In *Proc. of the AAS/AIAA Spaceflight Mechanics Meeting 2015* (pp. 1473–1492).

Letizia, F., Colombo, C., & Lewis, H. (2015b). Analytical model for the propagation of small-debris-object clouds after fragmentations. *Journal of Guidance, Control, and Dynamics*, *38*(8), 1478–1491. doi:10.2514/1.G000695.

Letizia, F., Colombo, C., & Lewis, H. (2015c). Multidimensional extension of the continuity equation method for debris clouds evolution. *Advances in Space Research*, *57*(8), 1624–1640. doi:10.1016/j.asr.2015.11.035.

Letizia, F., Colombo, C., Lewis, H. et al. (2018). Development of a debris index. *Astrophysics and Space Science Proceedings*, (pp. 191–206). doi:10.1007/978-3-319-69956-1_12.

Liou, J.-C., Hall, D., Krisko, P. et al. (2004). Legend – a three-dimensional leo-to-geo debris evolutionary model. *Advances in Space Research*, *34*(5), 981–986. doi:https://doi.org/10.1016/j.asr.2003.02.027.

McInnes, C. R. (1993). An analytical model for the catastrophic production of orbital debris. *ESA Journal*, *17*, 293–305.

McInnes, C. R. (1994). Compact analytic solutions for a decaying, precessing circular orbit. *The Aeronautical Journal*, *98*, 357–360. doi:10.1017/S0001924000026920.

McKnight, D. (1990). A phased approach to collision hazard analysis. *Advances in Space Research*, *10*(3), 385–388. doi:10.1016/0273-1177(90)90374-9.

McKnight, D., & Di Pentino, F. R. (2013). New insights on the orbital debris collision hazard at geo. *Acta Astronautica*, *85*, 73–82. doi:https://doi.org/10.1016/j.actaastro.2012.12.006.

Nazarenko, A. I. (1997). The development of the statistical theory of a satellite ensemble motion and its application to space debris modeling. In *Proc. of the 2nd European Conference on Space Debris* (p. 233). volume 393.

Smirnov, N., Kiselev, A., & Nazarenko, A. (2002). Mathematical modeling of space debris evolution in the near earth orbits. *Moscow University Mechanics Bulletin*, *57*, 33–41.

Smirnov, N., Kiselev, A., Nazarenko, A. et al. (2020). Physical and mathematical models for space objects breakup and fragmentation in hypervelocity collisions. *Acta Astronautica*, *176*, 598–608. doi:10.1016/j.actaastro.2020.02.050.

Smirnov, N., Kiselev, A., Smirnova, M. et al. (2015). Space traffic hazards from orbital debris mitigation strategies. *Acta Astronautica*, *109*, 144–152. doi:10.1016/j.actaastro.2014.09.014.

Smirnov, N. N., Dushin, V. R., Panfilov, I. I. et al. (1993). Space debris evolution mathematical modelling. In *Proc. of the 1st European Conference on Space Debris*. volume 1.

Smirnov, N. N., Nazarenko, A. I., & Kiselev, A. B. (2001). Modelling of the space debris evolution based on continua mechanics. In *Proc. of the 3rd European Conference on Space Debris* (pp. 391–396). volume 473.

Vallado, D. A., & McClain, W. D. (2007). *Fundamentals of astrodynamics and applications*. (2nd ed.). Dordrecht: Springer.

Walker, R., Martin, C., Stokes, P. et al. (2001). Analysis of the effectiveness of space debris mitigation measures using the delta model. *Advances in Space Research*, *28*(9), 1437–1445. doi:https://doi.org/10.1016/S0273-1177(01)00445-8.

Wittig, A., Colombo, C., & Armellin, R. (2017). Long-term density evolution through semi-analytical and differential algebra techniques. *Celestial Mechanics and Dynamical Astronomy*, *128*. doi:10.1007/s10569-017-9756-x.

Declaration of interests

☒ The authors declare that they have no known competing financial interests or personal relationships that could have appeared to influence the work reported in this paper.

☐The authors declare the following financial interests/personal relationships which may be considered as potential competing interests: